EVALUATION OF SENSITIZATION IN STAINLESS STEEL 304 AND 304L USING NONLINEAR RAYLEIGH WAVES

A Thesis
Presented to
The Academic Faculty

by

Christoph Doerr

In Partial Fulfillment
of the Requirements for the Degree
Master of Science in the
School of Civil and Environmental Engineering

Georgia Institute of Technology
December 2016

EVALUATION OF SENSITIZATION IN STAINLESS STEEL 304 AND 304L USING NONLINEAR RAYLEIGH WAVES

Approved by:

Professor Laurence J. Jacobs, Advisor
School of Civil and Environmental Engineering
Georgia Institute of Technology

Dr. Jin-Yeon Kim
School of Civil and Environmental Engineering
Georgia Institute of Technology

Professor Preet Singh
School of Materials Science and Engineering
Georgia Institute of Technology

Date Approved: 9 August 2016

ACKNOWLEDGEMENTS

First of all, I want to thank both my advisors Professor Laurence J. Jacobs and Dr. Jin-Yeon Kim. In particular, I want to thank Professor Jacobs for giving me the chance to come to Georgia Tech and being more than just a research advisor during the entire year. I want to thank Dr. Jin-Yeon Kim for giving me a lot of advice in the field of Rayleigh wave measurements and precipitate nucleation.

I want to give a special thank to Professor Preet Singh from the School of Material Science and Engineering at Georgia Tech for letting me use all of his lab equipment and giving me many insights about the sensitization process. Thank you for having always a solution to all my questions. Without your advice this research wouldn't have been possible. I'd like to thank Dr. Joe wall of EPRI for his insights and contributions. Further thank goes to Andrew Udell and his team in the CEE Machine Shop. Advising me with any issue about sample preparation and welcoming me many hours in their machine shop. Furthermore, I want to thank Professor Lothar Gaul and Christian Ehrlich from the Institute of Applied and Experimental Mechanics at the University of Stuttgart for organizing this program and choosing me as one candidate for this program. Thanks to my lab mates David Torello, Gun Kim, Katie Scott, Marc Forstenhauesler and Daniel Gruen. Especially, Marc Forstenhauesler for watching many real football games with me and Daniel Gruen for any stupid joke you have made. This made long lab days way more enjoyable. Thanks to Hannah Oerhmann for proof reading this Thesis.

Last but not least, I want to thank my family and my friends supporting me every day. This wouldn't have been possible without you.

TABLE OF CONTENTS

LIST OF TABLES

LIST OF FIGURES

LIST OF SYMBOLS

Symbol	Description
A, B	amplitudes
A_1	amplitude of fundamental frequency
A_2	amplitude of fundamental frequency
c	wave speed
C_{ijkl}	second order elastic modulus
C_{ijklmn}	third order elastic modulus
c_L, c_S, c_R	longitudinal, shear and Rayleigh wave speed
d	unit particle motion vector
E	Young's modulus
E	Lagrangian strain tensor
f	frequency
f_i	body forces
F	deformation gradient tensor
i	imaginary unit
k	wavenumber
M_{ijklmn}	Combination of second and third order moduli
n_i	normal vector
O	higher order terms
p	wave speed depending constant
p	unit propagation direction vector
P	Piola-Kirchoff stress tensor
s	wave speed depending constonat
S	surface
t_i	surface traction

Symbol	Description
u	displacement vector
V	volume
W	specific strain energy per unit mass
x	propagation distance
x	position vector
β	nonlinearity parameter
β'	relative nonlinearity parameter
δ_{ij}	Kronecker delta
ϵ	strain tensor
η	relative wave velocity
κ	relative wave number
λ	wavelength
λ, μ	Lamé constants
ν	Poisson's ratio
ρ	density
σ	stress tensor
θ_C	critical angle
φ, ψ	displacement potentials
ω	angular freqeuency
∇	Nabla operator
ξ	relative wave velocity

SUMMARY

Austenitic stainless steels have a wide range of applications in the energy industry, but the corrosion resistance of these stainless steels can be reduced by sensitization, which is the formation of chromium carbide precipitates at grain boundaries, causing the formation of a zone of chromium depletion at the grain boundary. Since chromium is the primary alloying element that makes stainless steel corrosion resistant, this chromium depleted zone is susceptible to stress corrosion cracking. Sensitization occurs when the stainless steel is exposed to a high temperature for an extended time period.

The objective of this research is to determine the sensitivity of nonlinear ultrasound to the presence of sensitization in austenitic stainless steels. This research uses nonlinear Rayleigh waves to quantitatively track the sensitization of SS304 and SS304L stainless steels as a function of holding time at 675 °C. The effect of the carbon contents of the alloys (SS304 versus SS304L) to the sensitization process and the measured nonlinearity parameters β' are investigated. An initial annealing of these specimens isolates the effect of just sensitization, removing the presence of cold work and residual stresses which can also affect the material nonlinearity. Complementary Electrochemical reactivation (EPR) measurements and microscopy are used to confirm the absence or presence of sensitization. These results show that the acoustic nonlinearity parameter is sensitive to the presence of chromium carbide precipitates. Furthermore, we investigated the sensitization process in the heat affected zone of a weld joint. The results show a dependency of the nonlinearity parameter β' to the distance from the weld joint.

CHAPTER I

INTRODUCTION

1.1 Motivation and Objectives

Austenitic stainless steels are creep and corrosion resistant materials that are commonly used in high temperature and chemical environments such as in oil and fuel pipelines or nuclear power reactors. These aggressive environments increase the risk of stress corrosion cracking (SCC) of austenitic stainless steels [36]. Many researchers have investigated the reasons and mechanisms leading to SCC. Sensitization, one reason for SCC, involves the depletion of chromium at the grain boundaries due the formation of chromium carbide precipitates when the steels are used in a temperature range from 450 °C to 850 °C. The carbide precipitation that is dominated by $Cr_{23}C_6$ is strongly dependent on the carbon and chromium content of the austenitic stainless steel used. Other factors, such as grain size, sensitization temperature and deformation also have a strong effect on the sensitization process. Nevertheless, many austenitic stainless steels are used in the temperature range between 450 °C and 850 °C and are strongly endangered by SCC because of sensitization [31]. Microcracks due to SCC can occur during the lifetime of a structural component and quickly grow once initiated. As these microcracks grow and join together, they become macrocracks which can lead to costly system failure. These macrocracks are often large enough to be detected by linear ultrasonic measurements using the scattered wavefield. Unfortunately microcracks, precipitates and dislocations are too small to be detected by linear ultrasound techniques, because their length scale is smaller than typical ultrasonic wavelengths [36]. Therefore, there is a need for techniques that can quantify the current state of structural components without affecting the operational schedule of the system, especially in nuclear power and pipeline industries. Quantitative nondestructive evaluation (NDE) of piping systems and infrastructure can avoid costly system shutdowns or catastrophic failure [8].

Previous research has demonstrated that nonlinear ultrasonic methods are sensitive to microstructural changes, and an early detection can lead to a longer lifetime and the avoidance of costly structural failures [25], [35], [18]. Many material developments were made to make pipelines and structural components more resistant to harsh environments. Austenitic stainless steels such as SS304 are widely used because of their low carbon content and higher resistance against SCC when compared to other carbon steels. But the SCC resistance of SS304 is still effected by chromium carbide precipitation at an operation temperature between 450 °C and 850 °C and adjacent to through-thickness welds [15]. The depletion of chromium due to the formation of these chromium carbides during sensitization makes this chromium depleted zone more susceptible to SCC. Considering the costs related to replacement or repair of structural components or system shut downs, it is necessary to get a deeper understanding of the sensitization mechanism and how it can be avoided [24]. The nucleation of these precipitates can be reduced by lowering the carbon content of the material used. Austenitic stainless steel SS304L has a lower carbon content compared to SS304. Therefore, sensitization should be less severe and slower compared to SS304.

The objective of this research is to determine the sensitivity of nonlinear ultrasound to the presence of sensitization in austenitic stainless steels. This is accomplished by investigating the effect of the different carbon contents between SS304 and SS304L and the effect of the precipitates on the measured nonlinearity parameter β'. Both materials are oven sensitized at 675 °C with different heat treatment holding times. After heat treatment, the effect of the chromium carbide nucleation is investigated using nonlinear ultrasonic Rayleigh wave measurements. Recent research has shown that these nonlinear ultrasonic measurements are sensitive to microstructure changes such as chromium carbide nucleation [15]. Initial annealing of these specimens isolates the effect of just sensitization, removing the presence of cold work and residual stresses which can also affect the material nonlinearity, so these sensitized specimens should only contain chromium precipitates in the grain boundaries. Therefore, changes in the measured nonlinearity parameter should only depend on the size and number of precipitates.

To support these measurements, complementary procedures measure the degree of sensitization (DOS) with the Electrochemical reactivation test (EPR) according to ASTM G108. This EPR test measures the amount of chromium depletion at the grain boundaries and gives an exact value of the DOS. By comparing the results of the ultrasound measurements and the EPR measurements, it is possible to correlate the changes of the measured nonlinearity parameter β' with the DOS. Furthermore, location, size and volume fraction of the chromium carbide precipitates are analyzed with microscopy images. Based on all these measurement results, it is shown that the nonlinear ultrasonic Rayleigh wave measurements can be used to quantitatively track the DOS in SS304 and SS304L. Furthermore, the Rayleigh wave measurement setup as well as the EPR test setup can be used to detect chromium carbide nucleation in the heat affected zone (HAZ) of a weld joint.

1.2 Structure of Thesis

The thesis introduces the problems of sensitization and stress corrosion cracking in austenitic stainless steels and provides the research objectives in chapter 1. Chapter 2 discuss the basic theory of the sensitization process. It describes the process of stress corrosion cracking as well as the sensitization process. Furthermore, it describes factors which contribute to the sensitization process. Chapter 3 illustrates the theoretical background of wave propagation in solids. Chapter 3 focuses on the propagation of

Rayleigh surface waves. Additionally, the fundamentals of nonlinear wave propagation and the effect of the material nonlinearity on a propagating Rayleigh wave are presented, including the nonlinearity parameter β. Chapter 4 provides information about the preparation of the used test samples. It illustrates the different chemical composition of the used materials as well as the different heat treatment times for the plate and welded samples. Furthermore, chapter 5 and 6 illustrates the setups and procedures of the Rayleigh wave measurements and the EPR measurements. Chapter 7 discusses the results of plate and weld samples. The nonlinearity parameter β' determined by Rayleigh wave measurements for these samples are shown. Furthermore, it provides EPR results as well as microscopy pictures to support the nonlinear ultrasonic results. Chapter 8 gives a conclusion about the research work and discusses possible future research based on this work.

CHAPTER II

STRESS CORROSION CRACKING AND SENSITIZATION

This chapter outlines SCC, sensitization and desensitization. The chapter briefly summaries the main reasons for SCC and focuses on sensitization and its chromium carbide precipitates, because this research focuses on the effect of sensitization in SS304 and SS304L. Generally, sensitization is the formation of precipitates at grain boundaries. However, we want to focus on carbide nucleation during the sensitization process, because $M_{23}C_6$ carbides are the main precipitates in the sensitization of austenitic steels as SS304 and SS304L.

2.1 Stress Corrosion Cracking

SCC is used to describe failures of engineering materials by environmentally induced crack propagating. SCC is the cracking of susceptible material that is used in a corrosive environment under tensile stresses. All three factors contribute to the risk of SCC. Figure 1 illustrates the key role of tensile stresses, corrosive environments as coastal areas and susceptible materials.

Furthermore, there are two different kinds of stress corrosion cracks depending on the PH value of the environment. All cracks with a PH value lower than 6 are associated with transgranular cracking. All cracks involving a PH value greater than 9 are associated with intergranular cracking. That means that the crack path of a transgranular crack is along the grain boundaries. Furthermore, a transgranular crack is just one big single crack path. The intergranular cracks also occur in the grain and increase with a higher temperature. In contrast, the transgranular cracks are not

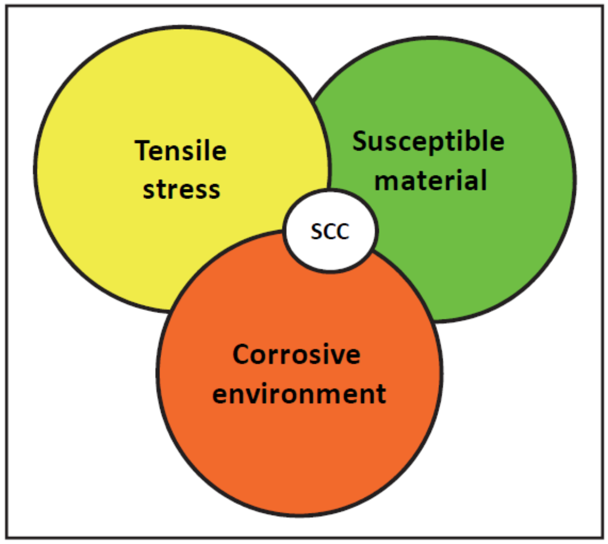

Figure 1: Influencing factors for SCC [8]

temperature dependent [8]. Figure 2 illustrates the two different crack types.

Intergranular cracks mostly occur in sensitized materials [19]. The sensitization process and the factors it depends on are described in the following section.

2.2 Sensitization

As mentioned in chapter 1, sensitization is highly undesirable and is necessary for SCC to occur. Therefore, engineers are trying to avoid sensitization by developing new materials. Sensitization is a highly complex process that depends on many different factors. Generally, sensitization is the formation of chromium carbide precipitates along the grain boundaries and the depletion of chromium in the vicinity. If the chromium content drops under 12 wt. %. in that area, these zones become vulnerable to corrosion [22]. Figure 3 illustrates the microscopy of a non-sensitized and sensitized SS304 material. The chromium carbide precipitates at the grain boundaries can be seen in figure 3. The sample of figure 3 is completely sensitized and almost every grain boundary is filled with precipitates.

First of all, the sensitization process depends on the carbon content of the material. Figure 4 shows a Temperature-Time-Sensitization curve. It illustrates that with a

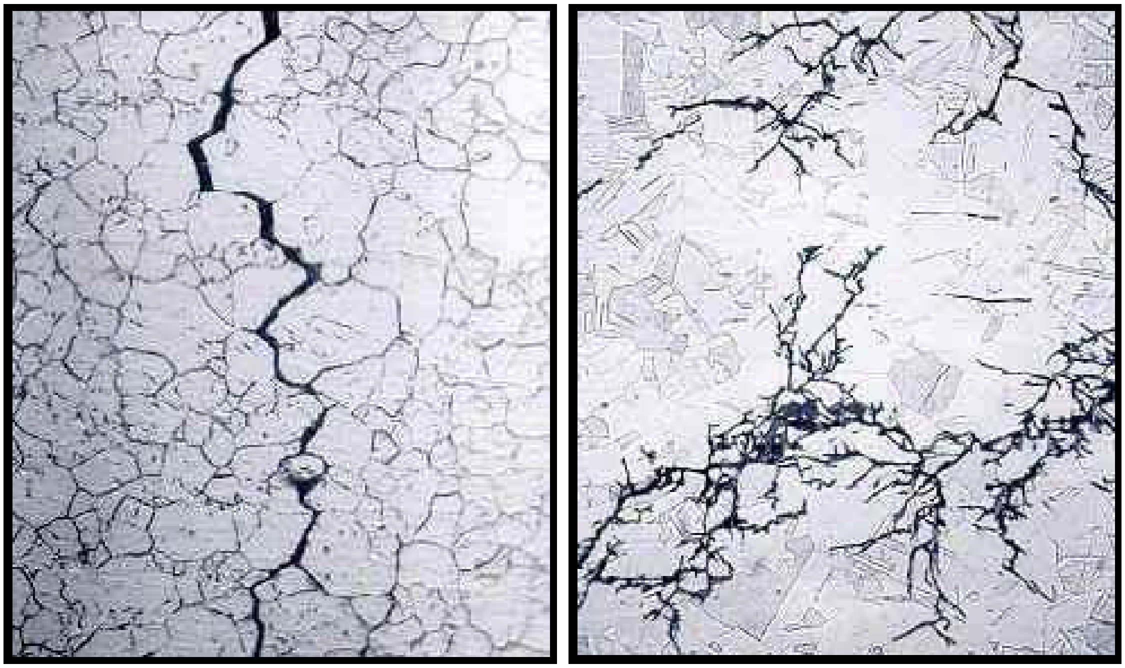

Figure 2: Transgranular(left) and intergranular(right) cracks [19]

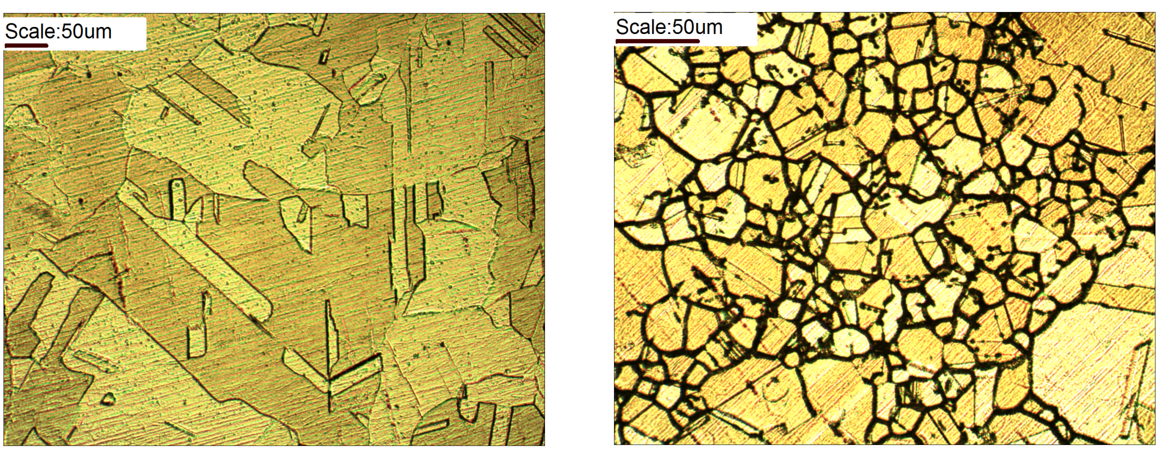

Figure 3: Microscopy of a non-sensitized sample and a sensitzed sample

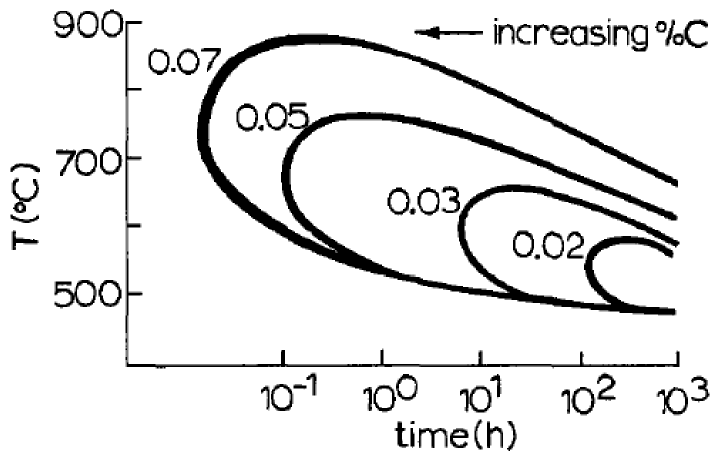

Figure 4: Temperature vs. time and carbon content [31]

decreasing carbon content, the maximum sensitization temperature decreases to 600 °C and the sensitization takes almost 100 hours.

Furthermore, Figure 4 shows the temperature dependence of sensitization. Figure 5 illustrates different total charges for different heat treatment times and temperatures. Chung et al. [7] have shown that DOS is strongly dependent on the heat treatment temperature and time. It can be seen that the DOS of the 650 °C heat treated specimen is higher than that for the 800 °C heat treated one. However, the 800 °C heated specimen has a higher rate of sensitization. Furthermore, figure 5 shows that sensitization starts earlier at 800 °C rather than at 650 °C. Chung et al. [7] have also investigated that chromium diffusion at 550 °C is very slow and the DOS is very low. However, a brief heating at 800 °C followed by a heat treatment at 550 °C caused a DOS almost as high as for the 650 °C specimen. The much higher carbide nucleation and chromium diffusion at 800 °C causes the high DOS for the combined (800 °C and 550 °C) heat treatment. Furthermore, a long preheating time at high temperature doesn't result in a further increase in the DOS. However, self healing of the material starts at longer heat treatment times at higher temperatures. This effect also takes place after 30 minutes at 800 °C. Figure 5 shows a decrease of the DOS which can be explained with desensitization, the self healing of the chromium

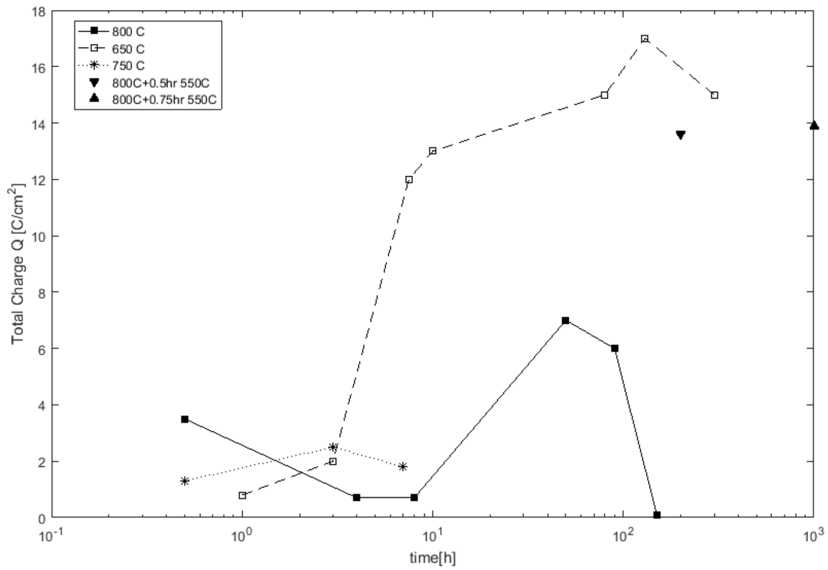

Figure 5: Total charge Q vs. heating time [7]

depleted zones. This also causes the decrease of the DOS at the end of every curve. The results of Chung et al. [7] are similar to those of other researches.

Kina et al. [13] have also shown a large difference in the DOS between a 650 °C and a 750 °C heat treated specimen. Figure 5 also illustrates the time dependency of sensitization. The carbide nucleation and the carbon diffusion need different times at different temperatures. The nucleation rate increases with a higher temperature, which explains the sharp increase of the "800 °C" curve at 30 minutes. However, the DOS is not increasing with a higher temperature.

Furthermore, the grain size affects the sensitization as well. A theoretical model has shown that carbide nucleation and sensitization kinetics are a function of the square of the grain size. By increasing the grain size, the sensitization process gets delayed at 600 °C and 650 °C. That effect causes a delay of desensitization as well. At 700 °C, the sensitization process gets accelerated with an increasing grain size. However, the desensitization process is pushed towards longer times. Generally, the sensitization domain gets bigger with an increasing grain size [24].

Besides the grain size, the grain orientation and boundary conditions affect the sensitization process. Kokawa et al. [14] investigated the grain boundary structure dependence on precipitation. They found out that some grain boundaries accept sensitization and others do not. Furthermore, they concluded that an ordered boundary needs either higher temperatures or more time for carbide precipitation. A higher difficulty in nucleation and a lower growth rate of carbides at more ordered grain boundaries causes this effect. Trillo et al. [32] examined how the misorientation angle of the grain boundaries affect the carbide precipitation. They have shown a preponderance of precipitates for higher misorientation angles. Therefore, deformation supports precipitation. Furthermore, with an increasing misorientation angle, the size of the precipitates increase and they have observed no precipitates on coherent twin boundaries. This means, that if there are no special boundary energies below the non-coherent twin boundaries there will not be any precipitates. It is important to know that sensitization will go on after finishing the heat treatment when choosing the right sensitization time. Generally, 234 K/h is a critical cooling rate. Therefore, every cooling rate that is smaller supports sensitization during cooling and every cooling rate that is higher does not. However, the critical cooling rate depends on the material and can vary from 234 K/h [21]. Besides the cooling rate, cold work has an effect on sensitization as well. Garcia et al. [9] have shown that different degrees of cold work influence the DOS. Figure 6 illustrates that with an increasing percentage of cold work the DOS increases as well. It can be seen that the total charge increases by more than 100%. Furthermore, it shows that the effect of cold work is independent on the heat treatment time.

Further aspects as the fraction of martensite and ferrit or alloy components also play a role for the sensitization process.

In conclusion, sensitization is a complex process that depends on many different factors. It is hard to focus just on one factor and estimate its influence, because all

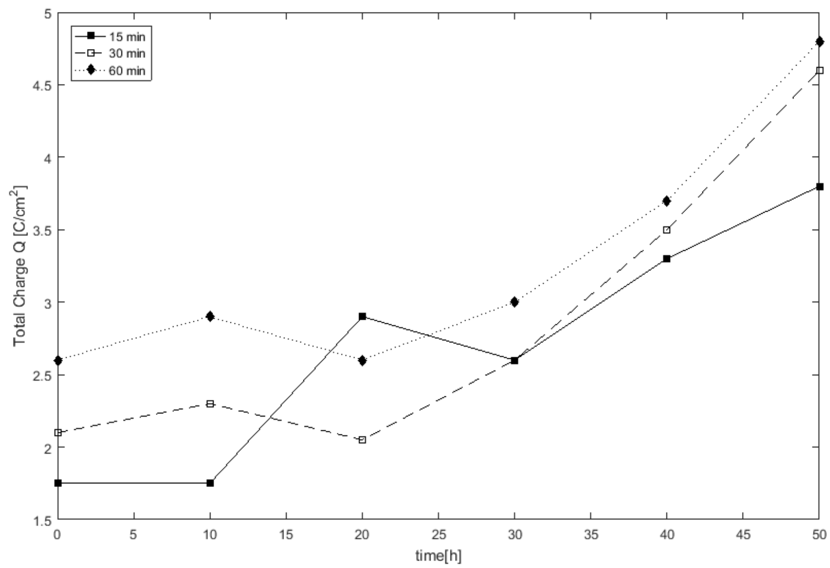

Figure 6: Total charge Q vs. cold work and different heat treatment times [9]

of them are influencing each other. Figure 7 shows how the carbon content, grain misorientation angle and the heat treatment time play a role in the sensitization process. With increasing carbon content, the carbide densitiy increases as well. However, the carbon density strongly depends on the misorientation angle. Therefore, it is important to consider all factors that affect the sensitization process.

2.3 Desensitization

Desensitization is not in the scope of this research, but sensitization and desensitization depend on each other. This section briefly describes the effect of desensitization. All the factors mentioned in section 2.2 influence the desensitization as well. With a delay in sensitization, desensitization gets pushed to longer heat treatment times. Figure 8 illustrates the DOS for different strain rates. It illustrates the increase during sensitization and the decrease during the desensitization.

Beltran et al. [6] have assumed that the sensitization-desensitization process follows a Gaussian deviation. Therefore, sensitization and desensitization time should be the same. This assumption has not been proven by further experiments.

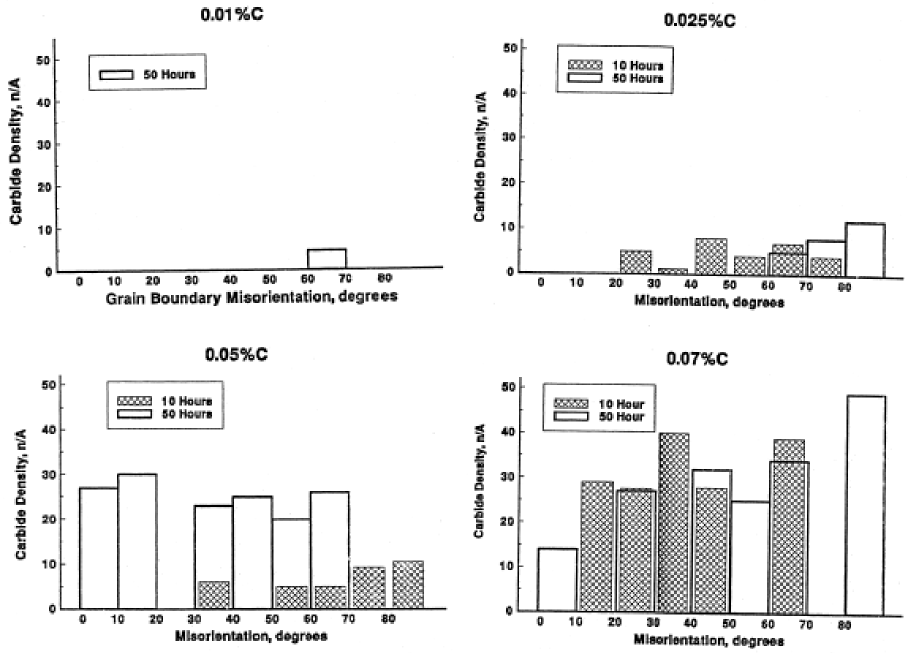

Figure 7: Carbide density vs. misorientation degree and carbon content [32]

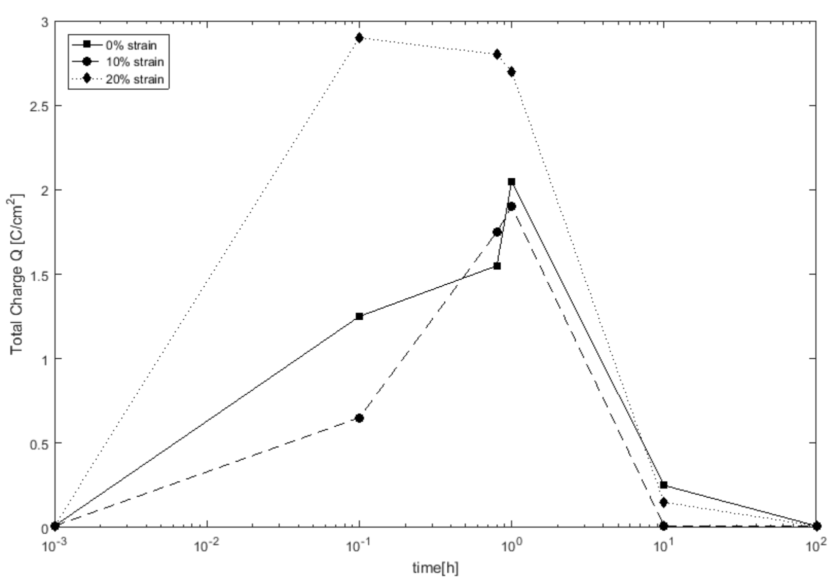

Figure 8: DOS vs. time [6]

CHAPTER III

WAVE PROPAGATION

This chapter provides an overview of the basic principles of wave propagation in elastic solids with a focus on ultrasound Rayleigh surface waves. Furthermore, it gives a brief summary of recent research works that has shown that nonlinear ultrasound measurements are sensitive to micro changes in material structures.

3.1 Equation of Motion

The derivation begins with the general form of the linear momentum balance, given by Aschenbach [2]

$$\int_S t_i \, dS + \int_V \rho f_i \, dV = \int_V \rho \ddot{u} \, dV. \tag{1}$$

In equation (1) S, and V refer to a surface and volume of a closed region of a body, respectivly. t_i and f_i express the surface traction and body force. Substituting t_i with the Cauchy stress definition

$$t_i = \sigma_{ki} n_k \tag{2}$$

into equation (2). n_k is the surface's normal vector component in k-direction. Applying the Gauss' theorem

$$\iint_S F_i n_i \, dS = \iiint_V \frac{\partial F_i}{\partial x_i} \, dV \tag{3}$$

to transform the surface integral into a volume integral and transfer it into the volume integral form

$$\int_V (\sigma_{ij,j})\, dV + \int_V (\rho f_i)\, dV = \int_V (\rho \ddot{u}_i)\, dV. \tag{4}$$

Equation (4) must hold for random V. Factoring out the integration to obtain Cauchy's first law of motion

$$\sigma_{ij,j} + \rho f_i = \rho \ddot{u}_i. \tag{5}$$

Using the relation of stress σ_{ij} and strain ϵ_{kl} for the linear elsatic case. The Cauchy stress σ_{ij} can be substituted and therefore it is just dependent on the displacement u using the fourth order eslastic stiffness tensor C_{ijkl}

$$\sigma_{ij,j} = C_{ijkl}\epsilon_{kl}. \tag{6}$$

Equation (6) shows the linear elastic relationship. Simplifying the stress-strain relationship for an isotropic and homogenous material, the elastic stiffness tensor can be characterized by two independent constants. The Lamé constants λ and μ are defined as

$$\lambda = \frac{E\nu}{(1+\nu)(1-2\nu)} \tag{7}$$

and

$$\mu = \frac{E}{2(1+\nu)}. \tag{8}$$

Involving the material constonts Young's modulus E and Poisson's ratio ν. That provides the simplified stress-strain relationship

$$\sigma_{ij} = \lambda\epsilon_{kk}\delta_{ij} + 2\mu\epsilon_{ij}. \tag{9}$$

Furthermore, the strain ϵ can be expressed in terms of displacement u with

$$\epsilon_{ij} = \frac{1}{2}(u_{i,j} + u_{j,i}). \tag{10}$$

Putting equation (7),(8) and (10) into Cauchy's first law of motion (5) and neglecting body forces f_i leads to Navier's euqation of motion, that is a differential equation just depending on a displacement u

$$(\lambda + \mu)u_{j,ji} + \mu u_{i,ji} = \rho \ddot{u}_i \tag{11}$$

or as vector notation

$$\mu\nabla^2 + (\lambda + \mu)\nabla\nabla \cdot u = \rho\ddot{u}. \tag{12}$$

Equation (11) and (12) describe three coupled partial differential equations depending on material properties and the displacement u. Bringing up a scalar potential φ and a vectorial potential ψ, u can be expressed as

$$u = \nabla\varphi + \nabla \times \psi. \tag{13}$$

Furthermore, we can use Navier's equation to get uncoupled differential equations in terms of the scalar potential φ and the vector potential ψ

$$(\lambda + 2\mu)\nabla^2\varphi = \rho\ddot{\varphi} \tag{14}$$

$$\mu\nabla\psi = \rho\ddot{\psi}. \tag{15}$$

Equation (14) and (15) can be rewritten as

$$\nabla^2\varphi = \frac{1}{c_L^2}\ddot{\varphi} \tag{16}$$

$$\nabla^2\psi = \frac{1}{c_S^2}\ddot{\psi} \tag{17}$$

with

$$c_L = \sqrt{\frac{\lambda + 2\mu}{\rho}} \tag{18}$$

$$c_S = \sqrt{\frac{\mu}{\rho}} \tag{19}$$

Equation (18) and (19) express the longitudinal c_L and the shear wave c_S velocities. Equation (16) and (17) illustrate the equations of motion for a longitudinal and a shear wave traveling in a linear-elastic, isotropic and homogenous solid.

3.2 Linear Wave Propagation

The following section gives a brief overview about linear wave propagation. It discuss linear plane waves and the reflection of a plane wave at a stress free surface.

3.2.1 Plane Waves

A wave propagating through a medium with the velocity c in the direction of motion with the unit vector d, the unit propagation vector p and the position vector x can be illustrated with

$$u = f(x \cdot p - ct)d. \tag{20}$$

Substituting the plane wave equation (20) into the Navier's euqation of motion in absence of body forces (12) results in

$$(\mu - \rho c^2)d + (\lambda + \mu)(p \cdot d)p = 0. \tag{21}$$

Equation (21) is only satisfied with either

$$d = \pm p \tag{22}$$

or

$$p \cdot d = 0 \tag{23}$$

Equation (22) illustrates a longitudinal wave because the propagating vector p is parallel to the displacement vector u. Rearranging equation (21) gives the following velocity

$$c = c_L = \sqrt{\frac{\lambda + 2\mu}{\rho}}. \tag{24}$$

In case of equation (23), p and d are parallel. Therefore, solving euqation (21) for the velocity yields

$$c = c_S = \sqrt{\frac{\mu}{\rho}}. \tag{25}$$

Furthermore, the wavenumber k_n of a wave n with the frequency w_n and the velocity c_n is defined as

$$k_n = \frac{\omega_n}{c_n}. \tag{26}$$

3.2.2 Reflection of a Plane Wave at a Stress Free Surface

Aschenbach [2] describes the displacement of a longitudinal or shear wave for the two dimensional case as follows

$$u^{(n)} = A_n d^{(n)} exp[ik_n(x_1 p_1^{(n)} + x_2 p_2^{(n)} - c_t)]. \tag{27}$$

The index n identifies the different case of an incoming longitudinal wave and a vertically polarized shear wave traveling in the (x_1,x_2)-plane or a horizontally polarized shear wave traveling in the (x_1,x_3)-plane. A_n identifies the amplitude of the traveling wave. Generally, the boundary conditions for the incident wave at x_2=0 are σ_{12}=0 and σ_{22}=0. Figure (9) illustrates different cases of an incident wave at a stress free boundary.

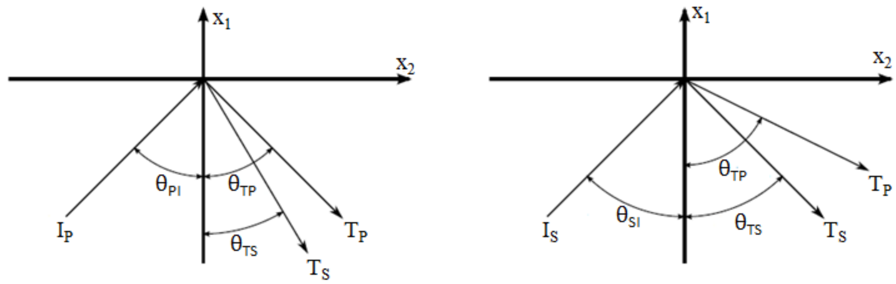

Figure 9: Reflection of a initial P-Wave or shear wave

The relation of an incident P-wave are $\theta_0 = \theta_1$ and $k_1 = k_2$. Furthermore,

$$k_2 = \frac{c_L}{c_S} k_0 = \kappa k_0 \tag{28}$$

and

$$sin(\theta_2) = \kappa^{-1} sin(\theta_0). \tag{29}$$

Here κ is

$$\kappa = \sqrt{\frac{2(1-\nu)}{1-2\nu}}. \tag{30}$$

For an incident shear wave, $\theta_0 = \theta_2$ and $k_2 = k_2$. Furthermore,

$$sin(\theta_1) = \kappa^{-1} sin(\theta_0). \tag{31}$$

There exists the special case of a critical incident angle θ_c for an incident shear wave, where just a shear wave will be reflected. The reflected longitudinal wave will travel along the surface of the second medium. This reflected longitudinal wave is called Rayleigh surface wave and plays a key role in this research. It will be discussed in the following section. The critical angle is defined as

$$\theta_c = arcsin \frac{c_s}{c_L}. \tag{32}$$

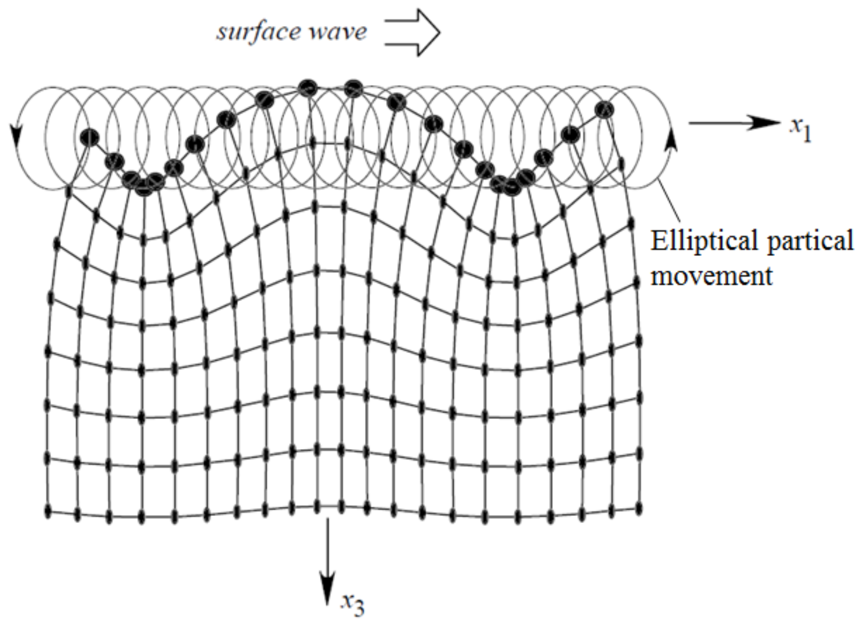

Figure 10: Rayleigh wave propagating in x_1 direction [33]

3.3 Rayleigh Surface Waves

As mentioned in the previous section, Rayleigh surface waves are a special case of a longitudinal wave. In 1885, Lord Rayleigh demonstrated theoretically that waves can propagate over the free surface of an elastic half-space. The amplitude of a Rayleigh surface wave decays with depth and the vibration is limited to a shallow layer of approximately one wavelength below the surface. Figure (10) illustrates the displacements of a two-dimensional Rayleigh wave traveling in x_1 direction. Furthermore, it shows the elliptical path of one particle. The amplitude of the displacement u_1 is dependent on the x_3 displacement.

The normal and tangential displacement components can be written as followed

$$u_1 = iA(k_R e^{-\kappa_d x_3} - \zeta \kappa_S e^{-\kappa_s x_3}) \tag{33}$$

and

$$u_3 = -A(\kappa_d e^{-\kappa_d x_3} - \zeta k_R e^{-\kappa_S x_3}). \tag{34}$$

where

$$\kappa_d = \sqrt{k_R^2 - k_d^2} \tag{35}$$

and

$$\kappa_S = \sqrt{k_R^2 - k_S^2}. \tag{36}$$

k_R and k_S are the wavenumbers of the longitudinal and shear waves. The 90° phase difference between the normal and tangential displacements indicates that the particle trajectories are ellipses. This displacement field can be used to determine the well known Rayleigh equation.

$$\eta^6 - 8\eta^4 + 8(3 - 2\xi^2)\eta^2 - 16(1 - \xi^2) = 0 \tag{37}$$

with $\xi = \frac{c_S}{c_d} = \sqrt{\frac{1-2\nu}{2(1-\nu)}}$ and $\eta = \frac{c_R}{c_S}$. According to Viktorov [33] the solution of the Rayleigh equation can be approximated by

$$\eta \approx \frac{0.87 + 1.12\nu}{1 + \nu} \tag{38}$$

which leads to a Rayleigh wave velocity

$$c_R \approx \frac{0.87 + 1.12\nu}{1 + \nu} c_S. \tag{39}$$

It can be seen that the Rayleigh wave speed is independent of the wave frequency. Therefore, they are nondispersive. Aschenbach [2] illustrates that Rayleigh waves are negligible at a depth of twice the wavelength. Typical excitation frequencies in nonlinear nondestructive testing are between 1 MHz and 10 MHz. This leads to wavelengths between 0.3 mm and 3 mm for steel, which has a Rayleigh wave velocity of $c_R \approx 2960\frac{m}{s}$. Therefore, every evaluated specimen should be at least 6 mm thick.

3.4 Nonlinear Wave Propagation

The linear wave propagation theory explained in section (3.2) is an idealistic assumption. The linear stress-strain relationship is valid for homogenous and isotropic medium when the applied stress is infinitesimal. Usually, materials in nature follow the nonlinear stress-strain relationship [34]. It has been shown ([30], [28], [19]) that this nonlinearity can be investigated and used to evaluate materials.

3.4.1 Theory of Nonlinear Wave Propagation

Starting with the equation of motion of a solid element in the absence of body forces

$$\rho\frac{\partial^2 u_i}{\partial t^2} = \frac{\partial \sigma}{\partial x}. \tag{40}$$

where u_i is defined as $u_i = x_i^* - x_i$. Using the deformation gradient tensor

$$F = \frac{\partial x^*}{\partial x}. \tag{41}$$

We can define the Lagrangian strain tensor as

$$E = \frac{1}{2}(F^T \cdot F - I) \tag{42}$$

or in index notation

$$E = \frac{1}{2}(\frac{\partial u_i}{\partial x_j} + \frac{\partial u_j}{\partial x_i} + \frac{\partial u_k}{\partial x_i}\frac{\partial u_k}{\partial x_j}). \tag{43}$$

Additionally, introducing the first Piola-Kirchhoff stress tensor

$$P = \frac{\rho_0}{\rho}\sigma \cdot F^{-T}. \tag{44}$$

ρ_0 refers to the density of the non deformed body and ρ to the density of the deformed body. Putting equation (44) into the equation of motion (5) leads to

$$P_{ij,j} = \rho_0 \ddot{u}_i. \tag{45}$$

The specific strain energy per unit mass W of the elastic body is defined as

$$P = \rho_0 \frac{\partial W}{\partial F} \tag{46}$$

and can be used to rewrite equation (44) as

$$P = \rho_0 F \frac{\partial W}{\partial E}. \tag{47}$$

Hamilton and Blackstock [10] assume for small strains the following expansion:

$$\rho_0 W = \frac{1}{2!} C_{ijkl} E_{ij} E_{kl} + \frac{1}{3!} C_{ijklmn} E_{ij} E_{kl} E_{mn} + O. \tag{48}$$

O refers to higher order terms and can be neglected for small strains. C_{ijkl} and C_{ijklmn} are the second and third order moduli. Using equation (43) and (48), the Piola-Kirchoff stress can be rewritten as

$$P_{ij} = C_{ijkl} \frac{\partial u_k}{\partial x_l} + \frac{1}{2} M_{ijklmn} \frac{\partial u_k}{\partial x_l} \frac{\partial u_m}{\partial x_n}, \tag{49}$$

where

$$M_{ijklmn} = C_{ijklmn} + C_{ijln}\delta_{km} + C_{jnkl}\delta_{im} + C_{jlmn}\delta_{ik}. \tag{50}$$

Substituting equation (49) into equation (45) leads to

$$\rho_0 \frac{\partial^2 u_i}{\partial t^2} = \frac{\partial^2 u_k}{\partial x_j \partial x_l} (C_{ijkl} + M_{ijklmn} \frac{\partial u_m}{\partial x_n}). \tag{51}$$

Equation (51) can be reduced to a one-dimensional P-wave problem as followed

$$\frac{\partial^2 u}{\partial t^2} = A\frac{\partial^2 u}{\partial x^2} + B\frac{\partial^3 u}{\partial x^3}, \tag{52}$$

where A refers to the second order term, depending on the second order elastic modulus C_{ijkl} and B refers to the third order term coming from the second order modulus C_{ijkl} and the tensor M_{ijklmn}. Kim et al. [12] have considered a time harmonic plane wave $A_1 cos(kx_1 - wt)$. A_1 is the amplitude, k the wave number and ω the angular frequency. They have expressed a the time-harmonic wave for a small material nonlinearity as followed

$$\begin{aligned} u_1 &= \frac{1}{8}\beta k^2 A_1^2 x_1 + A_1 cos(kx_1 - \omega t) + \frac{1}{8}\beta k^2 A_1^2 cos[2(kx_1 - \omega t)] + ... \\ &= A_0 + A_1 cos(kx_1 - \omega t) + A_2 cos[2(kx_1 - \omega t)] + ... \end{aligned} \tag{53}$$

Therefore, the nonlinearity parameter can be illustrated as

$$\beta = \frac{8A_2}{k^2 x_1 A_1^2}. \tag{54}$$

The nonlinearity parameter β and therefore equation (54) plays a key role in this research. β can be investigated by examining the amplitudes of the first and second harmonic wave traveling through the surface of a material. The change in β expresses the change of the amplitudes of the fundamental and second harmonic wave. Equation (52) has been solved for a one-dimensional longitudinal wave. However, Rayleigh waves are a combination of longitudinal and shear displacements. But, the acoustic nonlinearity for shear waves in an isotropic material is negligible due to the symmetry of the second and third order moduli [20]. Therefore, this research regards just material nonlinearity for longitudinal waves by measuring the amplitudes of the first and second harmonic wave at different propagating distances.

3.4.2 Nonlinear Rayleigh Waves

Restating the displacement field of a Rayleigh wave from section 3.4.1

$$u_1 = iA(k_R e^{-\kappa_d x_3} - \zeta \kappa_S e^{-\kappa_s x_3}) \tag{55}$$

and

$$u_3 = -A(\kappa_d e^{-\kappa_d x_3} - \zeta k_R e^{-\kappa_S x_3}). \tag{56}$$

Hermann et al. [11] has derived the displacement field of $u(2\omega)$ of the second harmonic Rayleigh wave traveling a sufficiently large distance as follows

$$u_1 \approx B_2(e^{-2px_3} - \frac{2ps}{k_r^2 + s^2} e^{-2sx_3}) e^{i2(k_R x_3 - \omega t)} \tag{57}$$

and

$$u_3 \approx iB_2 \frac{p}{k_R}(e^{-2px_3} - \frac{2k_R^2}{k_r^2 + s^2} e^{-2sx_3}) e^{i2(k_R x_3 - \omega t)}, \tag{58}$$

with

$$B_2 = \frac{\beta k_l^2 x_1 B_1^2}{8} \tag{59}$$

and

$$B_1 = -i\frac{2k_R p}{k_R^2 + s^2} C_1. \tag{60}$$

Putting equation (56), (58) and the derived equation (54) for the nonlinear parameter together yields to

$$\frac{u_3(2\omega)}{u_3(\omega)} = \frac{\beta k_l^2 x_1}{8i\frac{p}{k_R}(1 - \frac{2k_R^2}{k_R^2 + s^2})}. \tag{61}$$

$u_1(\omega)$ and $u_1(2\omega)$ refer to the displacement of the first and second harmonic Rayleigh wave. Solving equation (61) for the nonlinearity parameter β yields to

Table 2: Changes of β caused by micro structural changes

Mechanism	Change in β
Increasing dislocation density	$\Downarrow$
Increasing number of precipitates	$\Uparrow$
Precipitation radius and volume fraction increases	$\Downarrow$
Precipitates lose their coherency and volume fraction stays the same	$\Uparrow$

$$\beta = \frac{8ip}{k_l^2 k_R}(1 - \frac{2k_R^2}{k_R^2 + s^2})\frac{u_3(2\omega)}{xu_3(\omega)}. \tag{62}$$

In case of using a constant frequency the first part of equation (62) becomes a constant. Therefore equation (62) can be simplified to

$$\beta' = \frac{u_3(2\omega)}{xu_3(\omega)} = \frac{A_2}{xA_1^2} \approx \beta. \tag{63}$$

3.5 Application of Nonlinear Rayleigh Wave Measurements

Previous research works have shown that nonlinear Rayleigh wave measurements are sensitive enough to detect micro structural changes and plastic formation due to cold work, thermal aging, fatigue testing and creep [29]. Lakocy [15] has shown that the Rayleigh wave measurements can detect different carbide nucleation initiated by oven-sensitization and weld-sensitization. Table (2) illustrates the effect of different micro structural changes to the nonlinearity parameter β.

Therefore, Rayleigh surface wave measurements are perfectly suited to fulfill the purpose of this research. The upcoming chapters discuss the test samples, the different experimental set ups of this research and the results.

CHAPTER IV

TEST SAMPLES

4.1 Material

The materials investigated in this research are the commonly used SS304 and SS304L stainless steel. Table 3 shows their different chemical compositions. The chemical compositions of both materials are quite similar. The main difference is the higher carbon content (0.0455 wt. %) of the SS304 in comparison to the SS304L (0.0185 wt. %), which should affect the chromium carbide nucleation during the sensitization process. Both materials were solution annealed and water quenched after annealing during the manufacturing process. The annealing temperature was between 1038 °C and 1150 °C.

4.2 Preparation of the Plate Test Samples

All test samples are prepared in the same way. Both the SS304 and SS304L test samples are cut out of one plate of SS304 or SS304L stainless steel to 152.4x50.8x12.7 mm (6x2x0.5 inch) test samples. The thickness of 12.7 mm fulfills the requirement of twice the wavelength and guarantees that the generated surface waves are pure Rayleigh waves. As section 3.4 stated, the test samples should be at least as thick as twice the Rayleigh wavelength. The length of 152.4 mm guarantees an easy measurement setup for the wedge and a minimum propagation distance of 50 mm of the

Table 3: Chemical composition in wt. % of SS304 and SS304L specimens

Chemical	C	Co	Cr	Cu	Mn	Mo	N	Ni	P
SS304	0.0455	0.1520	18.1115	0.4565	1.7330	0.3415	0.0745	8.008	0.325
SS304L	0.0185	0.2115	18.285	0.4225	1.7865	0.3890	0.0787	8.055	0.32

Table 4: Heating times and heating temperatures for different plate samples

Annealed Samples (30 mins at 1080 °C)												
Temp [°C]	675											
Time [min]	30	60	90	120	150	180	240	360	480	780	1440	1800
SS304	x	x	x	x	x	x	x	x				
SS304L						x			x	x	x	x

As-recieved Samples												
Temp [°C]	675											
Time [min]	30	150	210	360	450	900	1200	1500	2220	2520		
SS304	x	x	x	x								
SS304L	x	x			x	x	x	x	x	x		

air-coupled transducer without any reflection effects from the front edge of the specimen. All specimens are surface ground and polished with a brushing wheel. Surface grinding provides a clean and even surface. That is most important for the Rayleigh wave measurements, in order to avoid effects of an uneven geometry on nonlinearity. By cooling the specimens constantly we avoid any heating during surface grinding. Furthermore, we just take 0.0127 mm thickness off per cut. This ensures that there are no further heat effects to the surface. The brushing wheel guarantees a finish of a 1000 grit surface for the EPR measurements and microscopy. Details about the EPR measurements are given in chapter 6 and the microscopy process is done according to ASTM E407 [5]. The different heat treatment methods and times are illustrated by table 4.

Using different heat treatment times results in several precipitation stages of the material. The longer heat treatment times for the SS304L samples were chosen because of the smaller amount of carbon in the material. All samples are put in a preheated (675 °C) furnace, and then sensitized for the given holding time. All specimens are air cooled. The higher cooling rate of 234 K/h ensures that no further sensitization occurs during cooling. But the cooling rate is slow enough to avoid internal stresses which also can have effects on the nonlinearity parameter β'. After the heat treatment, the surfaces of the specimens are ground and polished again to

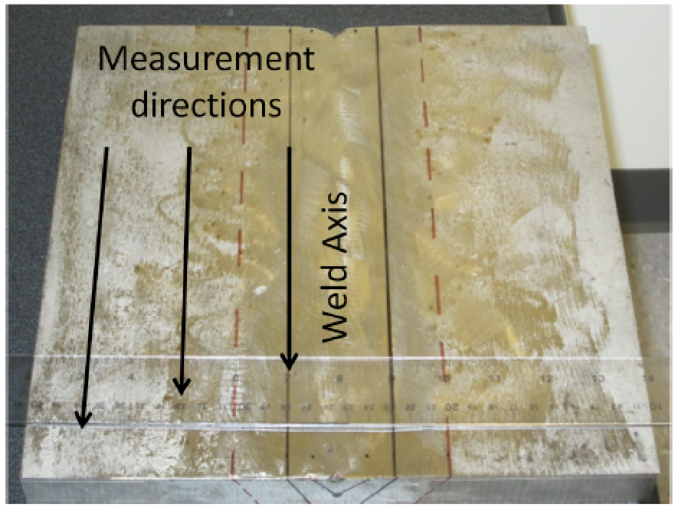

Figure 11: Plate with V-shaped cut, weld axis and measurement direction [15]

Table 5: Heating times and heating temperatures for the weld samples

Temp [°C]	675		
Time [min]	30	210	360
SS304 Weld Sample	x	x	x

remove the oxidized layer that is formed during the heat treatment.

4.3 Preparation of the Welded Test Sample

We used a welded stainless steel SS304 plate prepared by a V-notch, which was cut along the centerline and then welded full 15.88 mm deep and 50.8 mm wide with 308 stainless steel filler material with all four edges clamped. The top surface of the plate is flattened with a 55.8 cm diameter Blanchard grinder and finished with a cylindrical surface grinder. Afterwards, the top surface is polished with a random orbital sander and sanding block with sandpaper ranging from 50 to 800 grit. Figure (11) shows the stainless steel plate, the V-shaped cut, as well as the weld and the measurement direction. Details of the plate and its preparation are available in [15].

Table 5 illustrates the different holding times for the weld samples. We processed the Rayleigh wave measurements as well as the EPR measurements and microscopy between the heat treatments.

CHAPTER V

NONLINEAR ULTRASONIC RAYLEIGH WAVE MEASUREMENTS

This chapter describes the test setup and the test procedure for the nonlinear Rayleigh wave measurements that are used to measure the effect of the carbide precipitates on the nonlinearity parameter β'. The ultimate purpose of these measurements is to develop a system that can be used in the field. This field ready system should be capable of evaluating the material properties of structural components without affecting daily operations.

5.1 Experimental Setup

It is necessary to generate a wave packet to create the Rayleigh surface wave that interacts with the specimen. An Agilent 33250A 80MHz function generator is used to generate this wave packet. The output is a tone burst signal with a frequency of 2.1 MHz and a peak-to-peak voltage of 800 mV and length of 30 cycles with a burst period of 20 ms. Additionally, the function generator triggers the excitation amplifier and the oscilloscope. The generated sinusoidal signal is passed through a high power gated amplifier, a RITEC GA-2500A. The high power signal enables the transducer to introduce waves with a high acoustic energy to the material. This leads to a high signal-to-noise ratio (SNR) for the detection of the second harmonic wave at the air-coupled transducer. It is necessary to give this device a warm up time of 30 minutes. This ensures a stable output signal and a small amount of harmonic distortion in the created signal. This signal gets converted into a mechanical longitudinal wave by a broadband piezoelectric half inch transducer. This transducer has a nominal

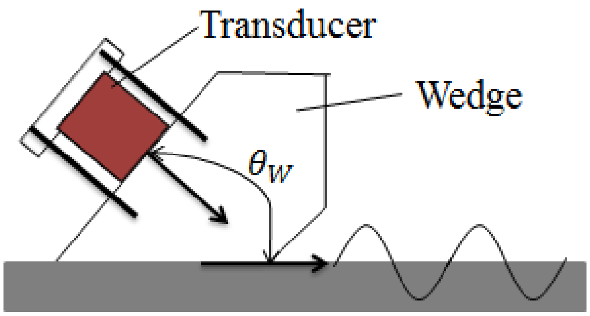

Figure 12: Wedge geometry

frequency of 2.25 MHz. The longitudinal wave has to be converted into a Rayleigh surface wave. This is achieved by using a Plexiglas wedge as shown in figure 12. By using Snells law and the known Rayleigh wave velocity in stainless steel and the longitudinal wave velocity in Plexiglas, the wedge angle can be determined with the following equation

$$\theta_w = arcsin \frac{c_p^{wedge}}{c_R^{specimen}}. \tag{64}$$

Figure 12 shows the wedge geometry, as well as the critical angle θ_w and the attached transducer. The transducer is clamped to the wedge by a plate and two set screws.

Furthermore, light lubricating oil is used to acoustically couple the transducer and the wedge, as well as the wedge and the sample. The clamping force between the transducer and the wedge, as well as the clamping force and clamping spot between the wedge and specimen have a significant impact on the measurement results. Therefore, it is necessary to create the same contact conditions for every measurement to get reproducible results by using the same amount of oil, the same clamping forces and clamping positions. Furthermore, settling effects influence the Rayleigh wave measurements. These settling effects are the results of changes of the oil film thickness and the resulting change of the clamping force. Therefore, it is necessary to let

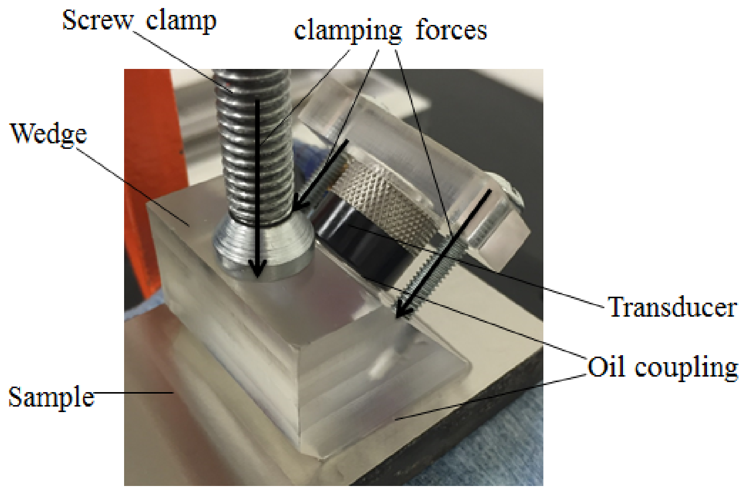

Figure 13: Wedge-specimen clamping condition

the entire setup rest for 30 minutes. Figure 13 shows the wedge-sample experimental setup.

After the Rayleigh surface wave traveled along the surface of the specimen, it has to be captured to measure the effect of the carbide precipitates on the second harmonic wave. An Ultran NCT4-D13 air-coupled transducer with a nominal center frequency of 4 MHz and an active diameter of 12.5 mm is used to detect leaked longitudinal waves in the air. As the Rayleigh surface wave starts propagating from the wedge along the surface of the specimen, the out-of-plane displacement of the surface material causes leaked pressure wave forms in the air close to the surface. These waves can be detected by the air-coupled transducer, which is sensitive to low energy ultrasonic longitudinal waves in air. Besides more repeatable measurement results, highly accurate positioning is the main advantage of the air-coupled transducer [28]. Figure 15 illustrates the 4 degrees of freedom of the air coupled transducer. The detected ultrasonic signal of the air-coupled transducer is converted into an electrical signal and carried to a Parametrics 5676PR pulse receiver to amplify the electrical signal by 40 dB without increasing the electrical noise. That signal travels to an oscilloscope

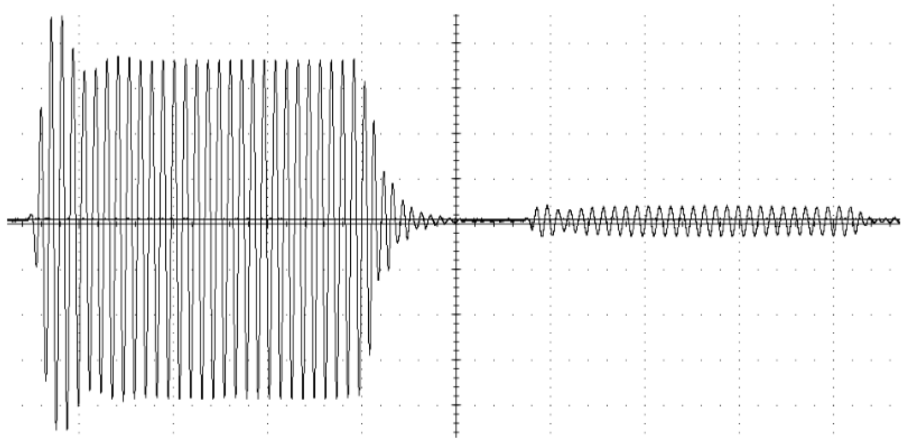

Figure 14: Captured signal of first and second harmonic wave

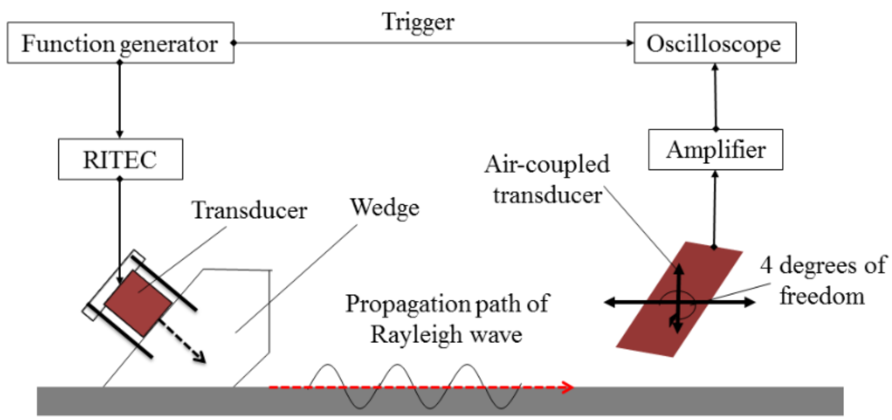

Figure 15: Test setup Rayleigh wave measurements

to capture the waveform. Figure 14 illustrates the captured signal of the first and second harmonic wave. 512 waveforms are averaged over one time-domain signal at each propagating distance. The captured signals are used for post-processing data analysis to compute the nonlinearity parameter β' and evaluate the impact of the chromium carbide nucleation. Figure 15 shows the entire test setup, as well as the connection between the test equipment. Furthermore, figure 16 illustrates how we realized the theoretical setup of figure 15. It shows the air-coupled transducer holder that obtains the 4 degrees of freedom of the air-coupled transducer.

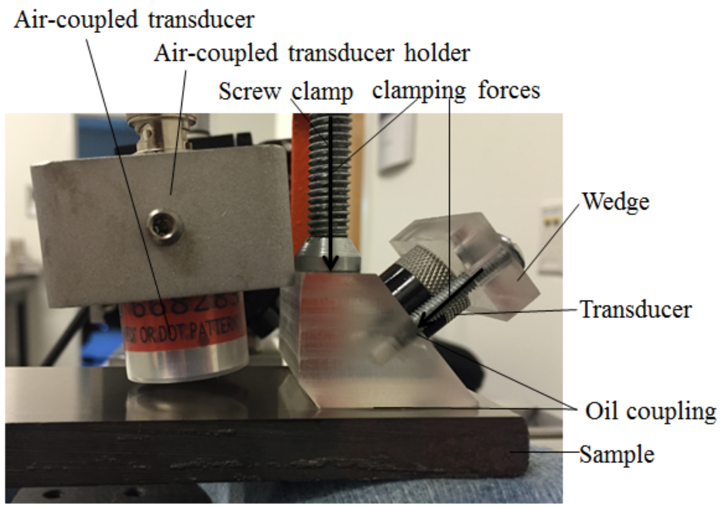

Figure 16: Wedge-Specimen-Air-coupled-transducer setup

5.2 Postprocessing Data Analysis

In order to calculate the nonlinearity parameter β', it is necessary to obtain the electrical signal amplitudes of the fundamental and second harmonic waves. Therefore, we need to map the time domain signal of the measured signal into the frequency domain. The steady state portion of the waveforms of figure 14 is identified and a Hann-Window is used to erase the ringing effects of the transducer. A peak detection code uses the middle 15 peaks of the signal. Therefore, it excludes the first eight and last seven. Those data points are affected by transient behavior of the piezoelectric transducers. By using a fast Fourier transformation (FFT) the signal is mapped into the frequency domain. Figure 17 shows the windowed and transformed A_1 and A_2 in the frequency domain as defined by equation (63).

Figure 18 illustrates the amplitudes of the fundamental and second harmonic waves over the propagation distance. As already discussed, it illustrates the decreasing of the fundamental amplitude A_1 for an increasing propagating distance. Furthermore, figure 18 shows the increase of the second harmonic amplitude A_2 with an increasing propagating distance.

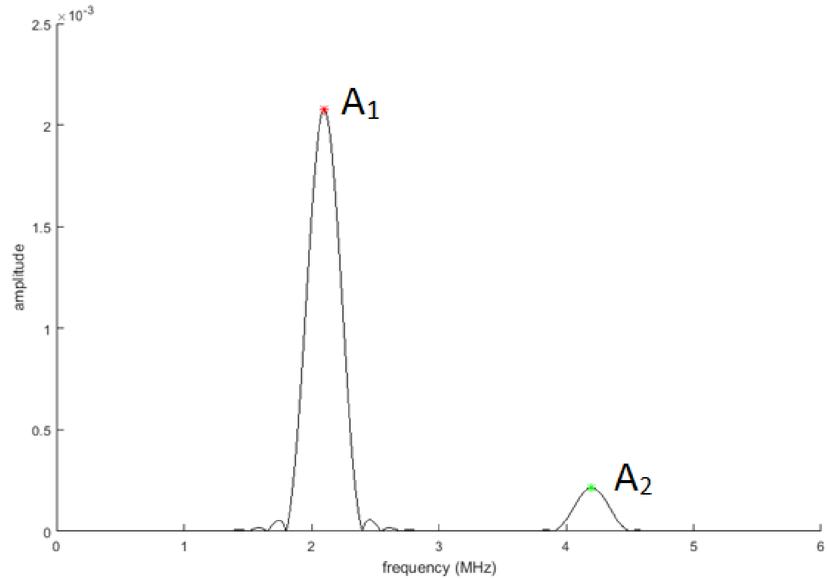

Figure 17: A_1(red star) and A_2(green star) transformed into frequency domain

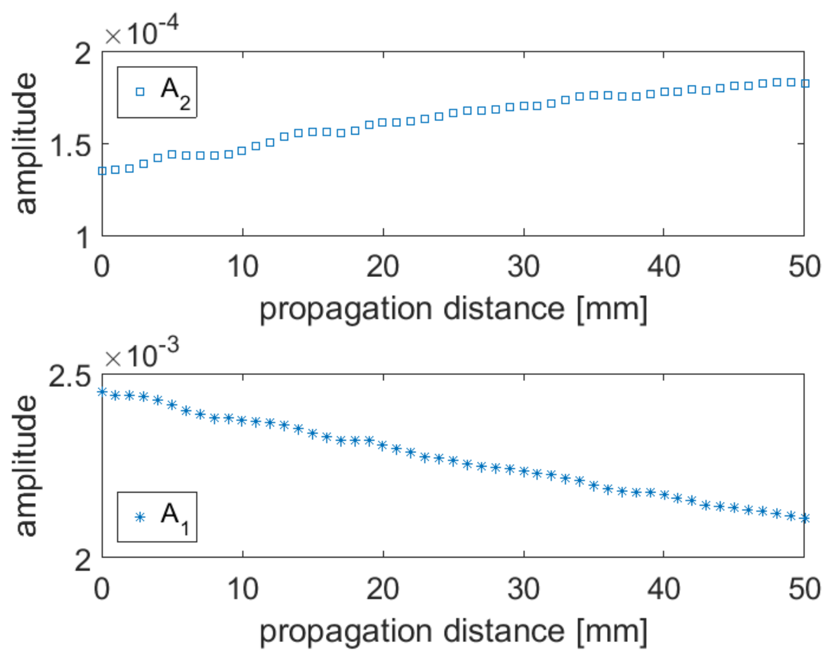

Figure 18: A_2 and A_1 vs. propagation distance

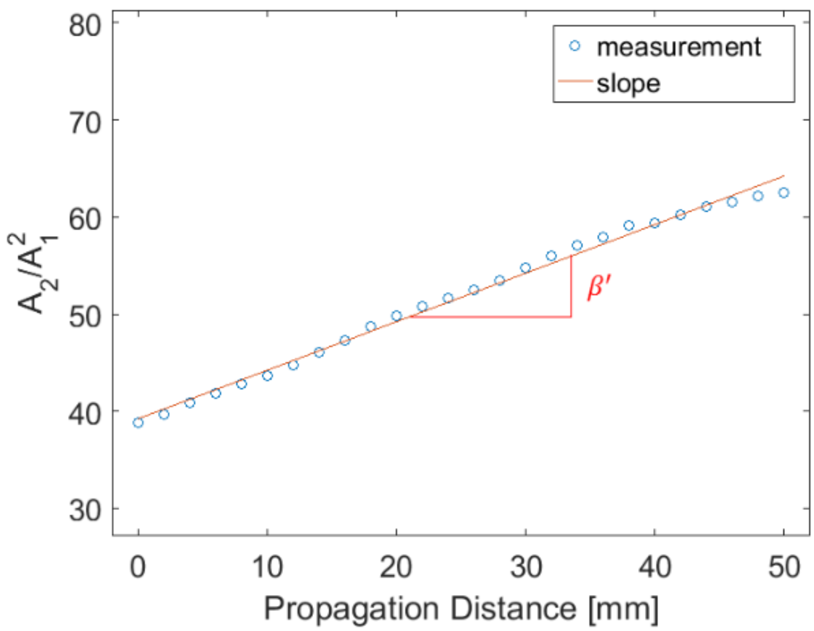

Figure 19: β' vs. propagation distance

Using these amplitudes to plot A_2/A_1^2 against the propagating distance. This plot illustrates several measurement dots that increase roughly linearly. Furthermore, the relative nonlinearity parameter β' can be calculated by using a linear fit through the measurement points. Figure 19 shows the nonlinearity parameter β' over the propagating distance with the actual measured A_2/A_1^2.

Furthermore, the R^2 value gives insight into the discrepancy between the measurement points and the linear fit. A good R^2 value is roughly 0.980 or higher.

5.3 Nonlinearity of the Measurement System

All electric components used such as the transducer, function generator, amplifier and coupling devices contribute to the measured nonlinearity. The goal of this research is to isolate the effect of carbide precipitates on the second harmonic wave. The material nonlinearity, created by carbide precipitates, increases with propagation distance. However, the nonlinearity of the system setup stays constant for the entire measurement. Therefore, the linear fit introduced in section 5.2 is just proportional but not

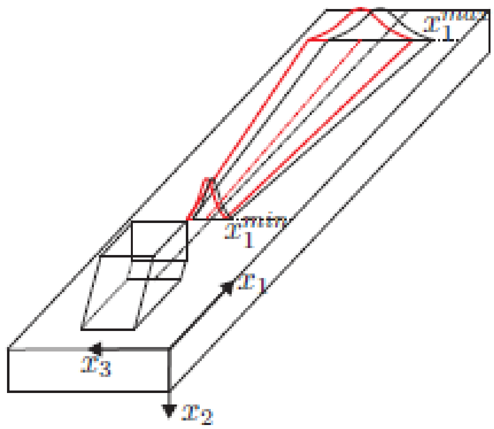

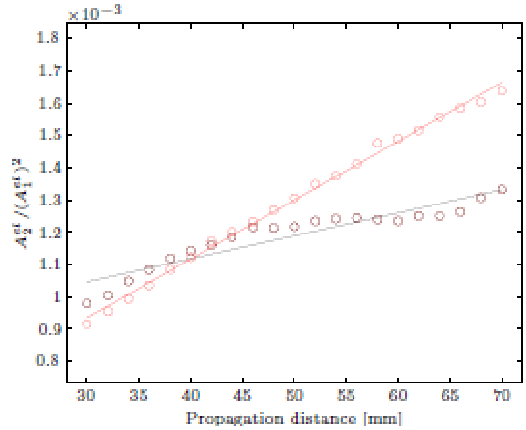

Figure 20: Expected straight(black) and actual(red) wave propagation(left) and β' for expected(black) and actual(red) wave propagation(right) [28]

equal to the material nonlinearity parameter β, because the transducer measures an electric signal that is dependent on the coupling conditions, frequency response of the transducer and the distance between air couple transducer and specimen. This leads to the introduction of the relative nonlinearity parameter β', which is calculated by using the measured electrical output,

$$\beta' \approx \frac{A_2^{(el)}}{A_1^{2(el)}} \propto \beta. \tag{65}$$

This research just compares the relative data of the nonlinearity parameter β'. However, this is still useful to compare the changes of β' for different heat treated specimens.

5.4 Measurement Procedure

After setting up all essential equipment parts for the nonlinear Rayleigh wave measurements and letting the setup settle for 30 minutes, the main measurement procedure can take place. The measurement estimates the change of the amplitudes of A_1 and A_2 over a certain range of propagation distance. Following Thiele [28], it is necessary to do an angular and path calibration. Figure 20 shows the alignment of the expected straight and the actual propagating path of the Rayleigh wave.

Thiele [28] has shown that the Rayleigh wave beam has a Gaussian profile, but fabrication discrepancy and uneven clamping forces cause a propagating path, which is not exactly perpendicular to the wedges' line source. Therefore, the Gaussian profile is just an ideal assumption. Measurements over the x_3 direction showed, that this Gaussian profile gets influenced by noises, the wedge geometry and measurement uncertainties. Therefore, it is necessary to measure the waves' peak value to calibrate start and end point of the x_3 direction. This indicates, that we always need to measure the peak of the propagating wave. The angular calibration of the air-coupled transducer leads to a maximum of the SNR. This Rayleigh wave angle α_R depends on the Rayleigh wave propagation speed and the P-wave speed in air. It has a value of 6° for steel. All three calibration steps use a set of measurements. The angle calibration is accomplished by creating a set of measurements with different angles at the same propagation distance. The maximum of the Gaussian profile at the start and end point of the measurement procedure are measured by creating a set of measurements at different x_3 spots for the start and end x_1 spot. Figure 21 shows the change of the fundamental amplitude over x_3. The start and end point of the measurement are defined by choosing the greatest measurement point. The blue stars represent the different measurement points and the red line illustrates a parabolic fit. However, it is necessary to choose the highest value of the measurement points and not the peak value of the fit.

After calibrating, the actual nonlinearity measurement can take place. Therefore, the air-coupled transducer is moved along the propagation distance at the peak of the Rayleigh wave. By changing the x_1 and x_3 position of the air-coupled transducer and measuring the amplitudes of the first(A_1) and second harmonic(A_2) waves, the relative nonlinearity parameter β' can be measured. Figure 20 illustrates two different A_2/A_1^2 vs. propagation distance. The red one is for the calibrated x_1 direction and the black one for the straight propagation distance by just calibrating the peak value

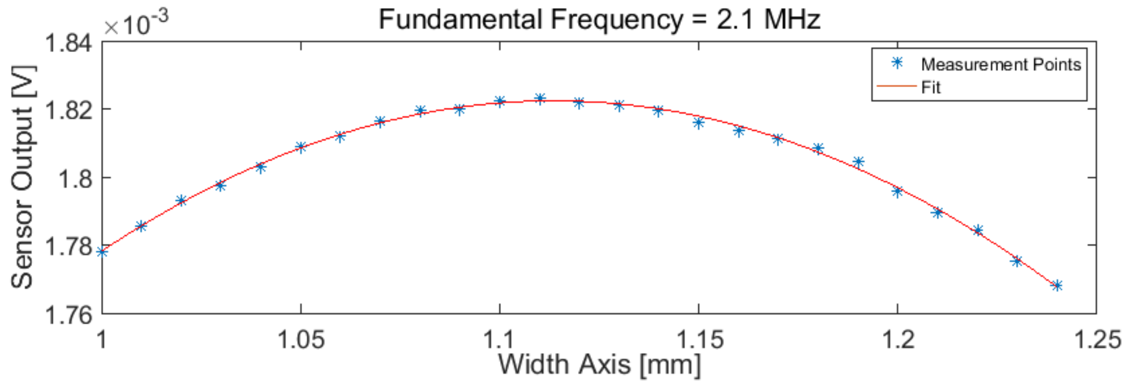

Figure 21: Start calibration for varying x_3

of the start point. This shows how important the calibration of the right start at end peak value is.

CHAPTER VI

EPR TEST MEASUREMENTS

This chapter gives a brief outline about the electrochemical reactivation (EPR) test method. It describes the background knowledge about the EPR, the test setup and test procedure.

6.1 Background

To estimate the DOS and support the results of the nonlinear Rayleigh wave measurements, we used the ASTM G108 EPR measurement method [4]. DOS gives an exact value of the extension of chromium depletion along the grain boundaries that is caused by chromium carbide precipitates. Many authors tried to correlate this chromium depletion along the grain boundaries to three main characteristics, coverage of the grain boundary by precipitates; width; and depth of the carbide precipitates [23]. The EPR test has a wide application range to provide an absolute value for the DOS and the results correlate with other test methods that are used to evaluate sensitization. The method creates a potentiodynamic sweep from the passive to the active regions of electrochemical potential using a procedure called reactivation. It measures the amount of charge referred to the corrosion of the chromium-depleted regions surrounding chromium carbide precipitations. As mentioned in section 2.2, these precipitations are mostly located at the grain boundaries caused by the nucleation of carbon and chromium to chromium carbide precipitates. The carbon which is needed for the nucleation travels from the middle of the grain to the grain boundary during the sensitization process. But particles located in the grain will also contribute to the measured total charge. When the electrochemical potential changes from the passive to the active region, the chromium-depleted areas in sensitized steels react in

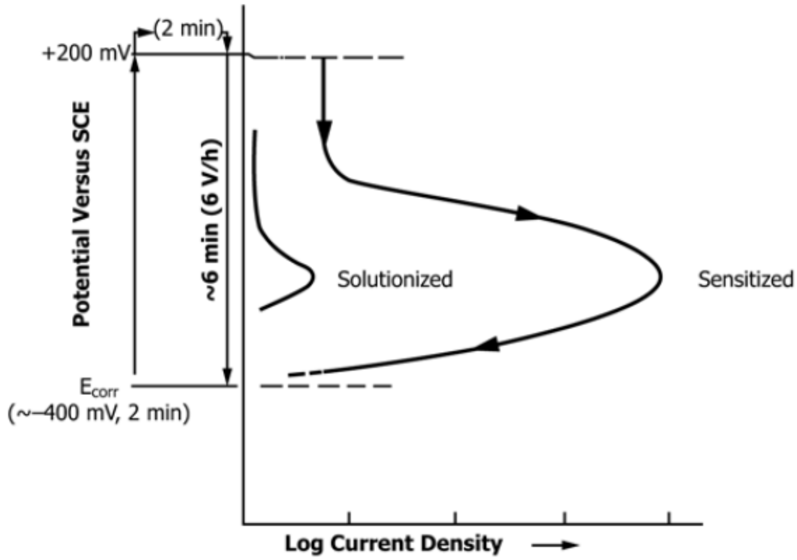

Figure 22: EPR test results for non-sensitized vs. sensitized steel [4]

oxidizing acid solutions. These areas are particularly susceptible to corrosion and this corrosion causes a rapid rise in the current density. Figure 22 illustrates the different rise of the current density between sensitized and non-sensitized stainless steel. The peak of the non-sensitized steel is very small compared to the peak of the sensitized steel.

Repeatability is one advantage of the EPR test method. Temperature, electrolyte composition and scan rate have to be controlled to get reproducible results [4].

6.2 Test Setup

Figure 23 shows the EPR test setup that is used in this research to make the EPR measurements. A typical EPR test setup consists of a scanning potentiostat, potential measuring instrument, current and current integration measuring instruments, test cell, specimen holder and test solution [4].

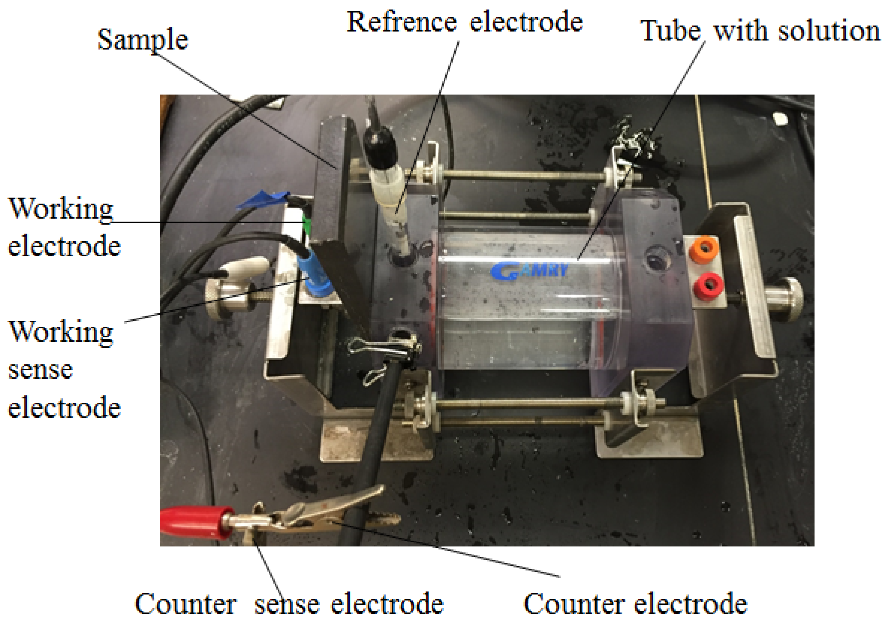

Figure 23: EPR test setup

6.3 Test Procedure

At first, the heat treated specimen has to be surface ground and polished after the sensitization heat treatment to remove oxidization products. It is important to remove any coarse scratches to get a homogenous surface. After preparing the test specimen it is necessary to prepare the test solution. The test solution consists of sulfuric acid H_2SO_4 and potassium thiocynate KSCN in reagent water. One liter of solution consists 0.5 mol H_2SO_4, 0.01 mol KSCN and one liter of distilled water. Before starting the reactivation scan, the open circuit potential has to be recorded. The potential has to be applied to the specimen for 2 minutes. The reactivation scan can be started after applying the potential to the specimen. Set the potential scan at a rate of 1.67 mV/s. The test instruments and test software measure the current density and create a potential-log-current-density diagram. We used a Gamry Refrence 600 potentiometer for the measurements and the Gamry Echem Analyst software to analyse the test results. We compare the peaks of the current density to the different heat treatment times and create the ratio to the peak of the untreated stainless steel samples. These results can be compared to the results of the nonlinearity parameter β' and a correlation between the increase of β' and the increase of the DOS can be created.

CHAPTER VII

RESULTS AND DISCUSSION

This chapter discusses all results of the nonlinear Rayleigh wave measurements, as well as the EPR measurements and the microscopy examination. It illustrates and discusses all results on their own, puts them in one context and tries to compare them, as well as finding a correlation between the Rayleigh wave measurements and the precipitate formation. As stated in chapter 4, we investigated samples as they were recieved from manufacturing (as-recieved samples) and we investigated annealed samples before sensitizing them in a preheated furnace. The results for the as-recieved and annealed samples are discussed in the following chapters. Furthermore, this chapter illustrates the Rayleigh wave and EPR results as well as the microscopy pictures of the weld-sensitized sample.

7.1 Results for SS304 and SS304L Plate Specimens

7.1.1 Rayleigh Wave Measurement Results

7.1.1.1 Results for Annealed Samples

This section shows the normalized β' results for the annealed samples. All shown Rayleigh wave results are normalized to the first measurement set at 0 minutes. Figure 24 illustrates the normalized nonlinearity parameter β' over different heat treatment times for the annealed SS304 samples. The figure shows a phase between 0 minutes and 120 minutes where β' stays almost the same. Any variations in β' during this phase is probably caused by measurement uncertainty. The measurement uncertainty of the Rayleigh wave measurements can also be seen in figure 24 and is about $\pm 5\%$. The measurement uncertainty is influenced by variabilities in the test setup. A different amount of oil, different clamping forces and different clamping

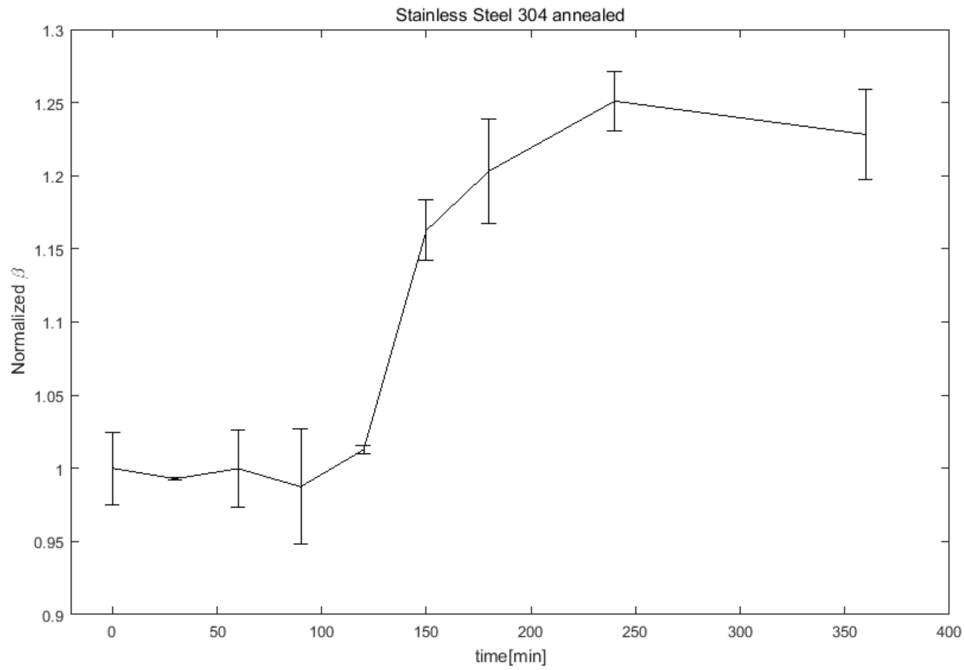

Figure 24: Normalized β' over different heat treatment times at 675 °C for annealed SS304

positions in each measurement. After 120 minutes at 675 °C β' increases rapidly. The value of β' increases in the next 30 minutes by 17% and then further 8% in the next 60 minutes. Therefore, the peak value at 240 minutes is 25.8% higher than before heat treating the SS304 plate at 675 °C.

This increase is caused by chromium carbide nucleation. The number and size of the precipitates increase with increasing heat treatment time and cause the increase in β'. This effect will also be discussed in section 7.1.2 and 7.1.3. After 240 minutes β' decreases slightly. Therefore, the SS304 is saturated and there is no further precipitate increase.

Figure 25 represents the normalized β' over different heat treatment times for the annealed SS304L samples. This figure illustrates the phase of steady state from 0 minutes to 180 minutes and a large increase by 16% in the next 300 minutes. The increase slows down afterwards and the peak value is reached at 1440 minutes. For the

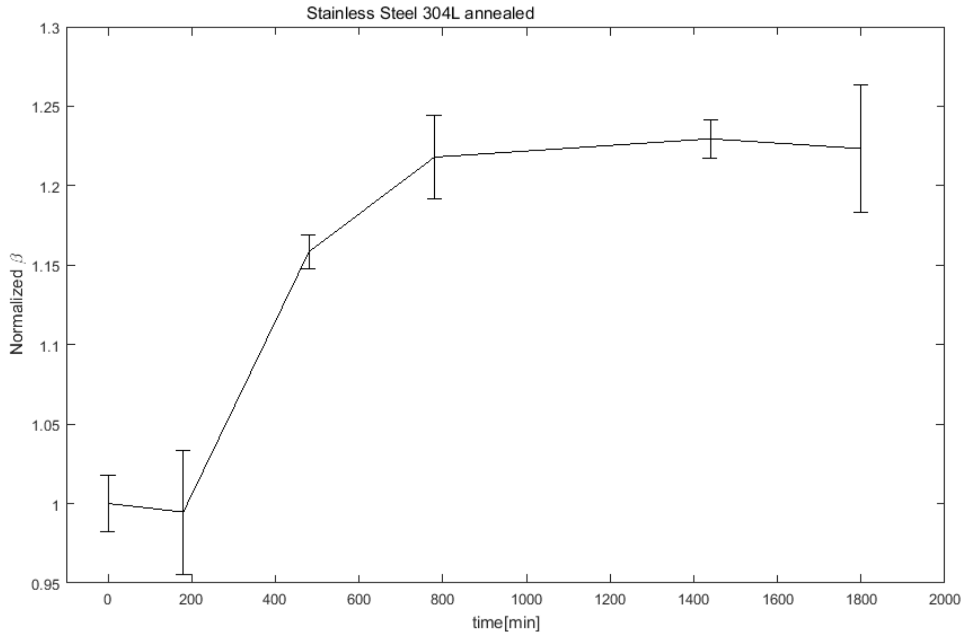

Figure 25: Normalized β' over different heat treatment times at 675 °C for annealed SS304L

SS304L the increase is about 24% from the starting point. Because β' just increases by 1% between 780 minutes and 1440 minutes, the sample is saturated after 780 minutes, with a total increase of almost 23%.

The sensitization process takes about 5 times longer for the SS304L than for the SS304. Furthermore, sensitization starts later for the SS304L — sensitization starts after 180 minutes for the SS304L and after 120 minutes for the SS304. Figure 26 illustrates the normalized β' over different heat treatment times at 675 °C for annealed SS304 and SS304L. Both have a steady-state phase at the beginning and then β' increases caused by chromium carbide nucleation. With longer heat treatment time the number and size of the precipitates increases which causes an increase in β' as well. It can be seen that the entire process takes longer for the SS304L than for the SS304. Because the temperature was the same for both the heat treatments, this difference is caused by the different micro structure of the materials, especially the lower carbon content of the SS304L. The lower carbon content of the SS304L causes

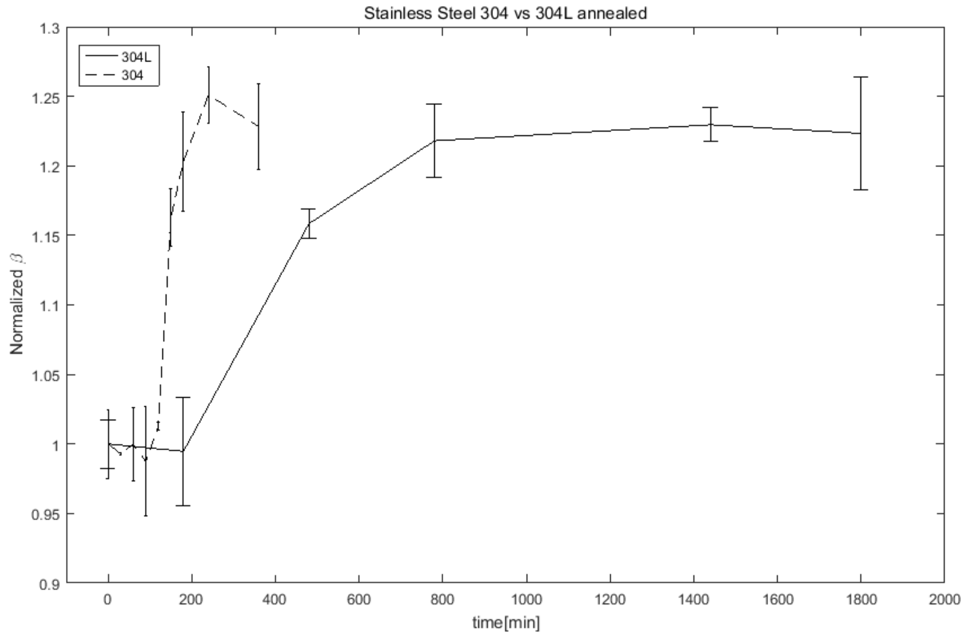

Figure 26: Normalized β' over different heat treatment times at 675 °C for annealed SS304 and SS304L

the longer sensitization time for the SS304L and the delayed start of sensitization. The results follow the overall trends for the SS304 specimen seen in [1], except the increase in β' seen in [1] is on the order of 60% as opposed to the 25% increase seen here.

7.1.1.2 Results for As-recieved Samples

Figure 27 illustrates the normalized β' for SS304 over different heat treatment times. It can be seen that β' drops for about 27% and increases between 30 and 150 minutes by 14.2%. After 150 minutes the β' value stays almost the same. A small decrease by 2% is shown. However, the 2% decrease after 150 minutes is in the range of the measurement uncertainty. After the saturation point at 150 minutes, the sensitization and carbide nucleation process is finished and the chromium carbide precipitates stop growing. Therefore, the nonlinearity parameter β' stops increasing as well. The initial drop of β' between 0 and 30 minutes is caused by stress relieving effects. As mentioned

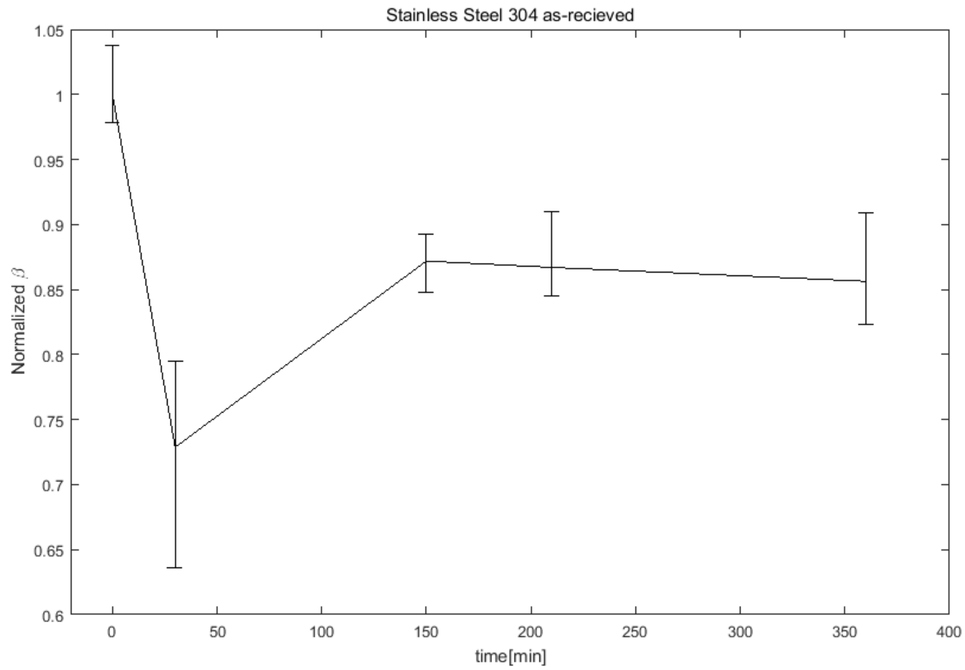

Figure 27: Normalized β' over different heat treatment times at 675 °C for as-recieved SS304

in chapter 4, during the manufacturing process the samples were water quenched after solution annealing. The water quenching process affects the micro-structure of the samples and increases the number of dislocations and internal stresses. Marino [17] has shown that in the first 30 minutes of a heat treatment at 650 °C, the number of dislocations decreases significantly, while the precipitates have not started to grow. In general, this stress relieving process causes the drop in β'. The increase by 14.2% after 30 minutes is caused by chromium carbide nucleation and occurs between 30 and 150 minutes.

Figure 28 illustrates the normalized β' results for SS304L over different heat treatment times. As in figure 27, the β' drops first and increases afterward. However, it takes 450 minutes of heat treatment to start the nucleation process that causes an increase in β'. The decrease takes 450 minutes and has value of almost 40%. The increase by 21% starts at 450 minutes and takes 1050 minutes.

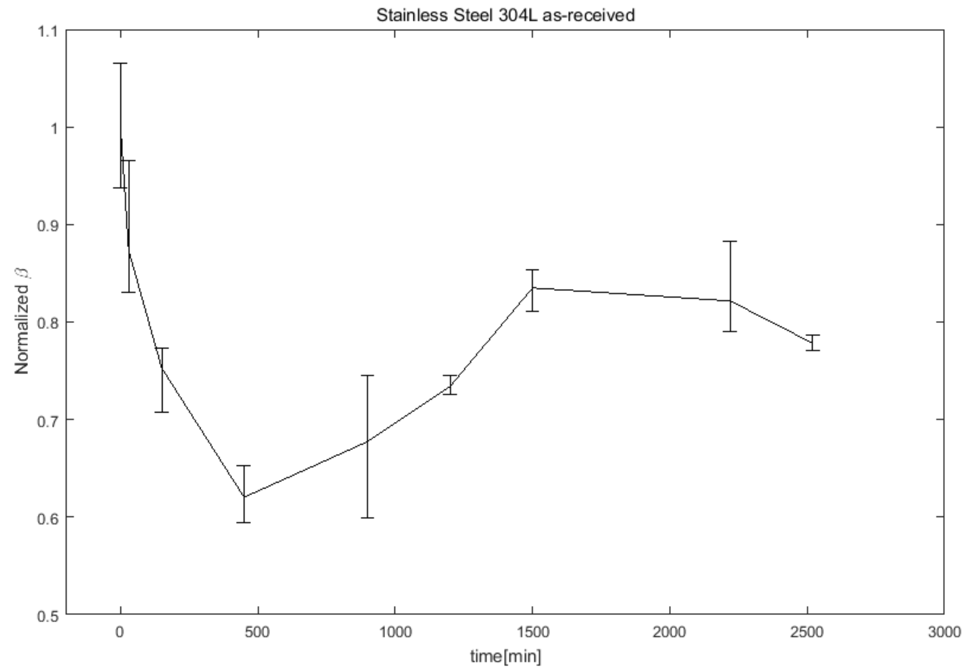

Figure 28: Normalized β' over different heat treatment times at 675 °C for as-recieved SS304L

Figure 29 shows the normalized β' of SS304 and SS304L over the heat treatment time in one plot. Both curves follow the same tendency. First they drop because of the decreasing number of dislocations and then β' increases due to chromium carbide nucleation. After the peak, β' decreases again, but not as much as at the beginning. It can be seen that the entire process takes longer for the SS304L than for SS304. The carbon diffusion to the grain boundary is slower by the factor 8.75 compared to SS304. It takes 120 minutes from the minimum at 30 minutes to the peak value at 150 minutes. In comparison, it takes 1050 minutes from the minimum to the peak value for the SS304L. Therefore, the SS304L has more time for relief, because it takes longer for sensitization to start. This leads to a deeper drop at the beginning by 40%.

7.1.2 EPR Results

Figure 30 illustrates the reactivation scan of a non-sensitized SS304 sample. Furthermore, figure 31 illustrates the reactivation scan of a sensitized SS304 sample. As

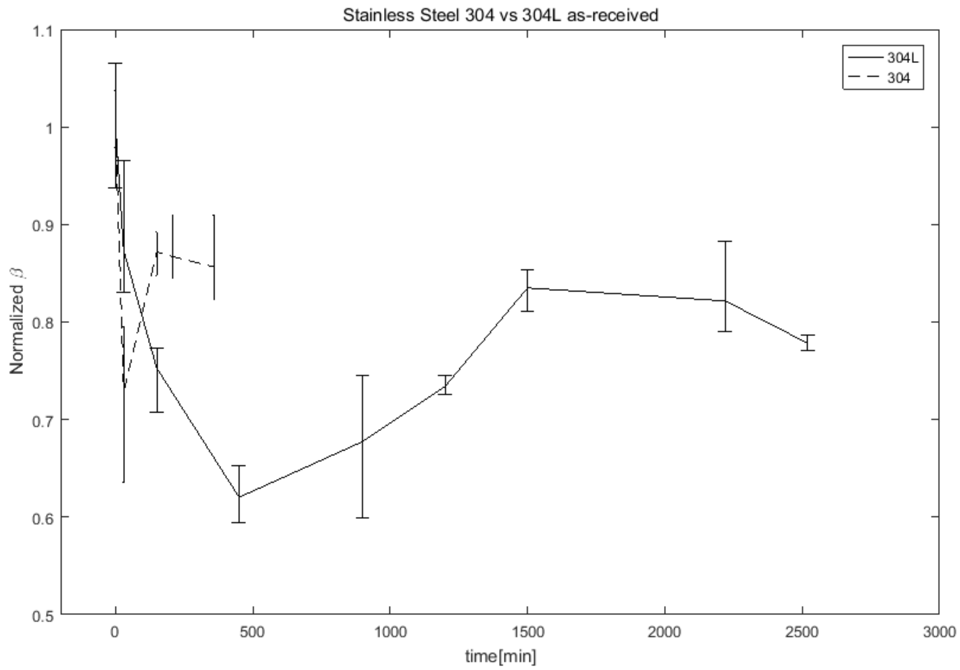

Figure 29: Normalized β' over different heat treatment times at 675 °C for as-recieved SS304 and SS304L

already mentioned, sensitized materials have a higher current density because of the bigger chromium depleted zones, which get activated by the EPR test. This higher current density peak can be seen in figure 31 compared to figure 30. We used the peak values of the reactivation scans to evaluate the change of the chromium depleted zones. All EPR results presented here are shown by the change of the current density normalized to the current density value of the 0 minutes heat treated sample.

7.1.2.1 Results for Annealed Samples

Figure (32) represents the different peak current densities over different heat treatment times for the annealed SS304 samples. It shows a small increase at the beginning, a strong increase between 150 minutes and 240 minutes. With longer heat treatment times, the carbide nucleation starts and the chromium depleted zones get larger. Therefore, the current density increases till the sensitization process is completed. The increase slows down at the end between 240 minutes and 360 minutes.

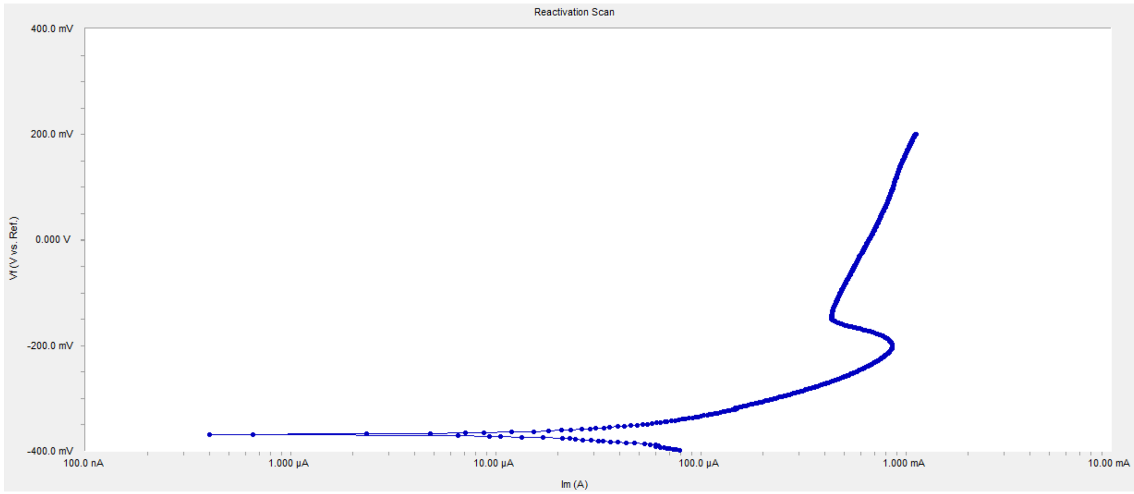

Figure 30: EPR Results for a non-sensitized sample

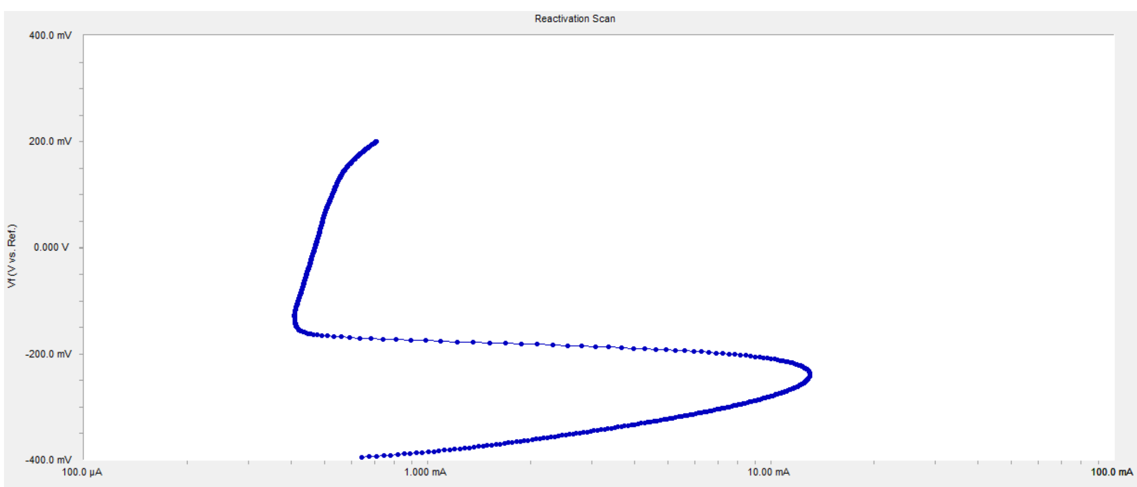

Figure 31: EPR Results for a sensitized sample

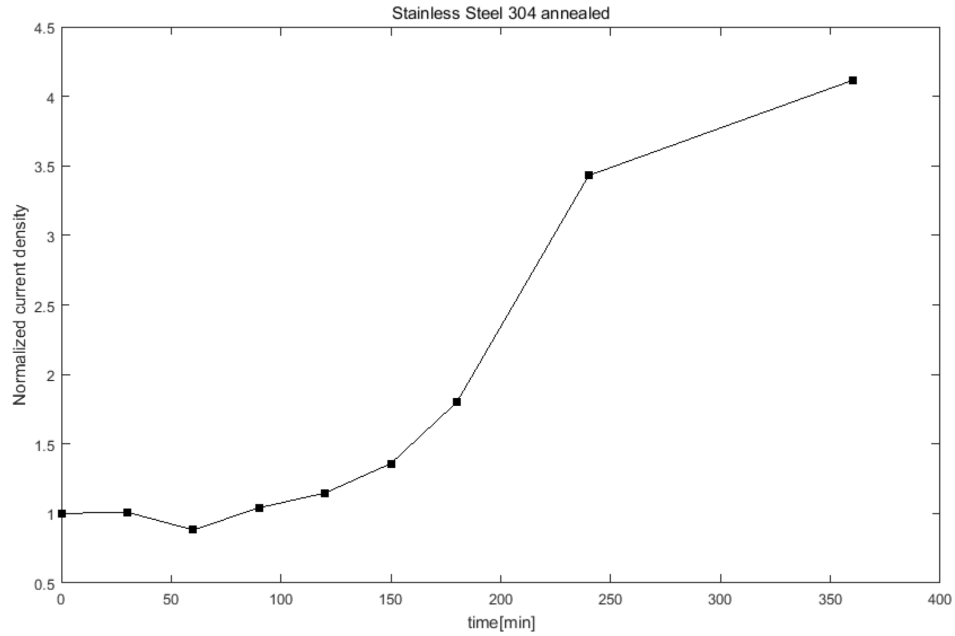

Figure 32: EPR Results over different heat treatment times for SS304 annealed samples

The total increase of the current density peak is 400%.

Figure 33 illustrates the different peak current densities over different heat treatment times for the annealed SS304L samples. It shows a steady increase from the beginning. The peak value is reached after 1440 minutes and is about 300% higher than for the 0 minutes sensitized one. If we would look at a current density value between 0 minutes and 100 minutes the value would probably not be as high as the curve in figure 32 illustrates. Figure 33 illustrates a slow increase at the beginning and a fast increase in the middle. In comparison, figure 32 shows a steady increase to the peak.

Figure 34 shows both EPR curves of the SS304 and SS304L annealed samples in one plot. As in section 7.1.1 described, it takes longer for the 304L to totally sensitize. Sensitization starts for both materials straight at the beginning, but the growth of the chromium depleted zones is slower for the SS304L than for the SS304. The difference between the peak values can also be explained with prior cold work during

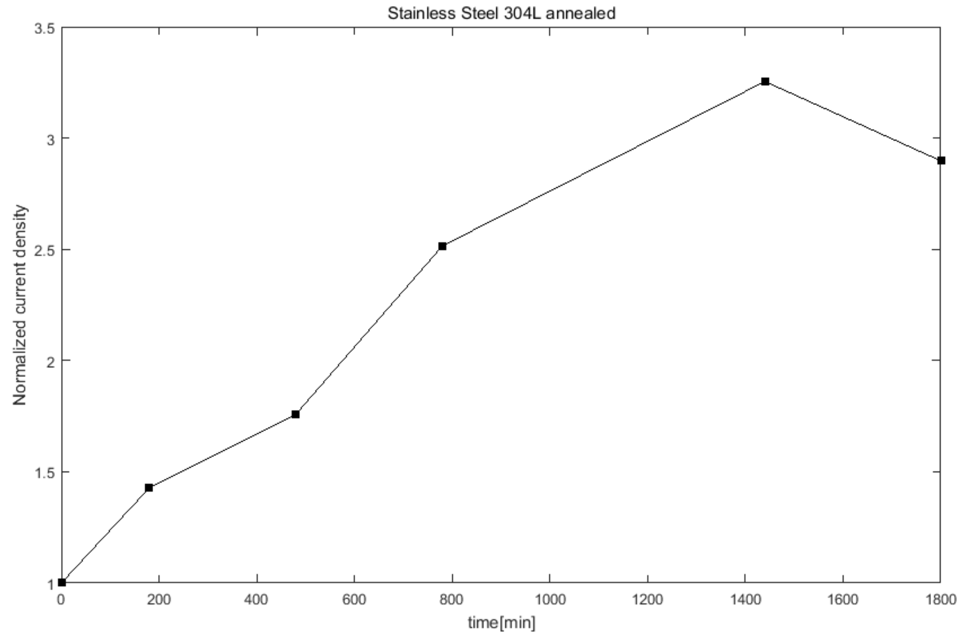

Figure 33: EPR Results over different heat treatment times for SS304L annealed samples

the manufacturing process. This cold work affects the martensite phase formation, which contribute to the sensitization process [9].

7.1.2.2 Results for As-received Samples

Figure 35 illustrates the EPR results for the as-received SS304 samples. It can be seen that the EPR curve follows the same trend as β' curve. There is a drop at the beginning of the heat treatment and after 30 minutes the curve rises to its peak at 210 minutes and drops again afterward. The drop at the beginning is also caused by a reduced number of dislocations, because the EPR test activates the chromium depleted zones as well as the dislocations. Therefore, by reducing the number of dislocations the current density gets reduced as well. Figure 35 shows the strong increase in current density in the middle and afterwards, desensitization starts and the curve drops again. Chromium from the middle of the grain travels to the grain boundary slower than carbon. This causes the nucleation of chromium carbides and

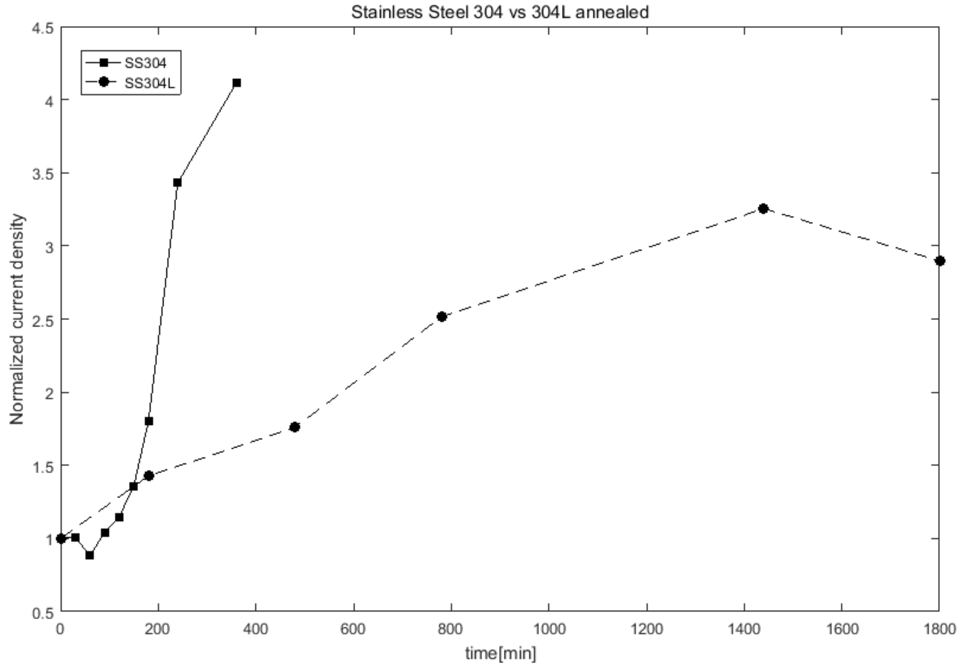

Figure 34: EPR results over different heat treatment times for SS304 and SS304L annealed samples

the rise of the DOS. The chromium arriving later near the grain boundary fills up the chromium depleted zone, and causes the drop at the end of the heat treatment. Therefore, the chromium depleted zones get smaller and with further heat treatment the chromium depleted zones would disappear as figure 8 represents. However, the precipitates formed still remain at the grain boundary which causes the steady-state phase of the nonlinearity parameter β' at longer heat treatment times.

Figure 36 shows the EPR results for the as-received SS304L samples. As in figure 35, the current density drops by almost 70% and increases constantly afterwards. Between 450 and 1500 minutes of heat treatment the fastest increase occurs and it slows down after 1500 minutes. However, it keeps increasing after 1500 minutes. We stopped the heat treatments after 2520 minutes because evaluating the effect of precipitation growth on the nonlinearity parameter β' is the main research objective and as seen in section 7.1.1 β' stays almost the same after 1500 minutes of heat treatment.

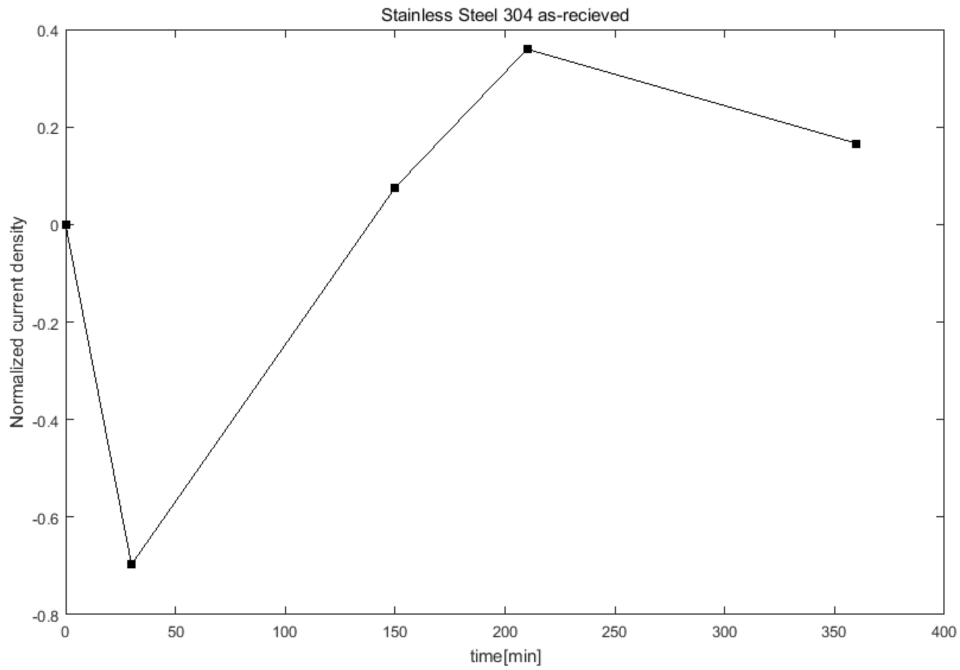

Figure 35: EPR results over different heat treatment times for SS304 as-recieved samples

Therefore, we did not continue the heat treatment to evaluate the desensitization process, because desensitization has no effect on the nonlinearity parameter β'. The total increase after 2520 minutes is 339%.

Figure 37 shows both EPR curves in one plot. As in section 7.1.1.2 described, it takes longer for the 304L to totally sensitize. Sensitization starts for both materials at 30 minutes, but the growth of the chromium depleted zones is slower for the SS304L than for the SS304. The difference between the peak values can be explained with prior cold work during the manufacturing process. This cold work affects the martensite phase formation, which contribute to the sensitization process.

7.1.3 Microscopy

This section illustrates the chromium carbide nucleation at different heat treatment times with microscopy pictures by etching the material according to ASTM 407. All figures 38,40,39,41 show the same trend. With increasing heat treatment time

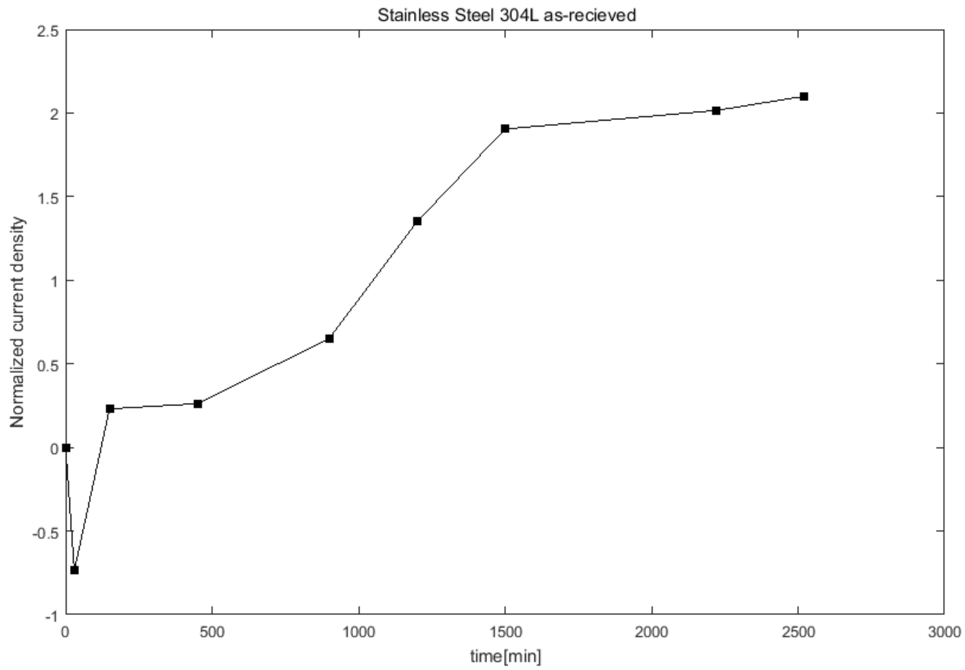

Figure 36: EPR results over different heat treatment times for SS304L as-recieved samples

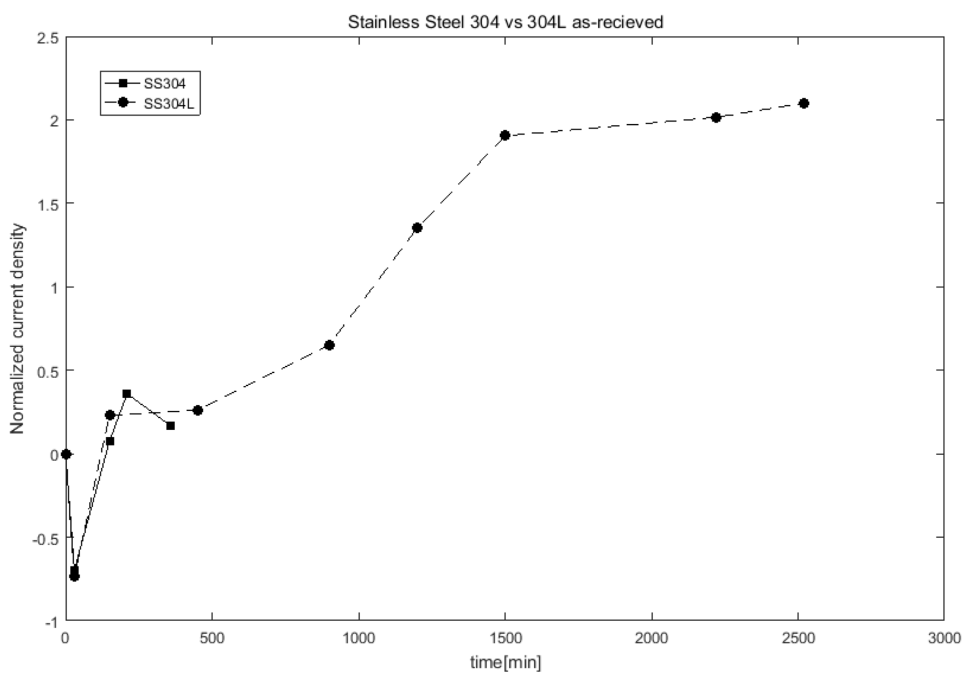

Figure 37: EPR results over different heat treatment times for SS304 and SS304L as-recieved samples

the numbers and the size of precipitates at the grain boundary increase and at the end, the number and size stagnate. This fact supports the nonlinearaty parameter β' results. Those β' also show an increase phase and a steady-state phase at the end. This steady-state phase of β' represents the saturation of size and numbers of precipitates. As already mentioned, the EPR results show either a further increase or a decrease at this phase caused either by further increase or a decrease of the chromium depleted zones. However, both behaviors do not affect the size and number of precipitates and therefore do not affect the β' value. Furthermore, the grain size increases during the annealing process. This grain size increase causes the delayed start of chromium carbide nucleation for the annealed SS304 samples, compared to the as-recieved samples. However, the grain size for the annealed SS304L samples is doubled as well, but sensitization starts earlier for those samples compared to the SS304L as-recieved samples. The high temperature of the annealing process achieves a faster stress relieving process. Therefore, sensitization starts earlier for the SS304L annealed samples.

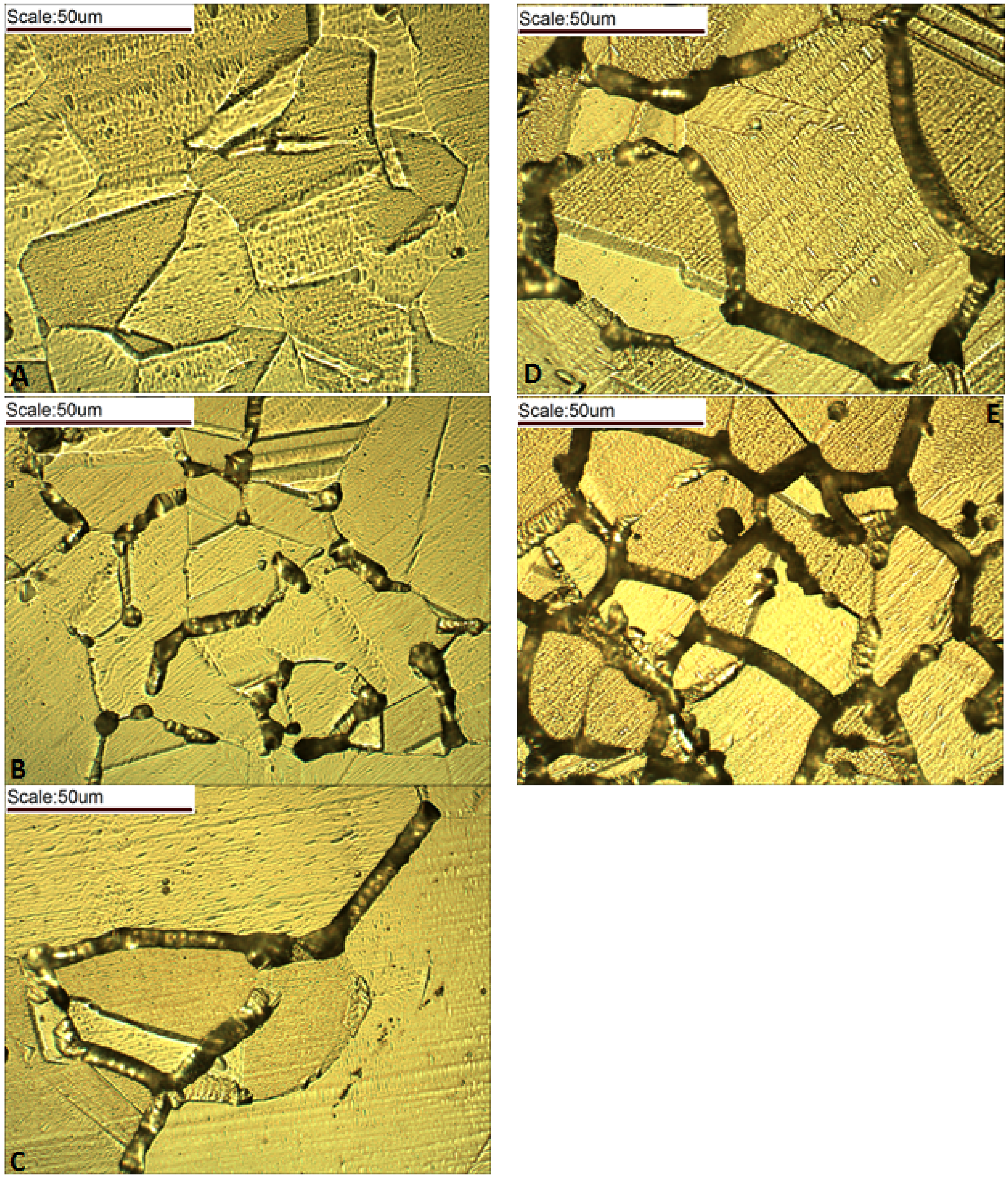

Figure 38: Microscopy for as-recieved SS304 samples at 0 minutes(A), 30 minutes (B), 150 minutes (C), 210 minutes (D) and 360 minutes (E)

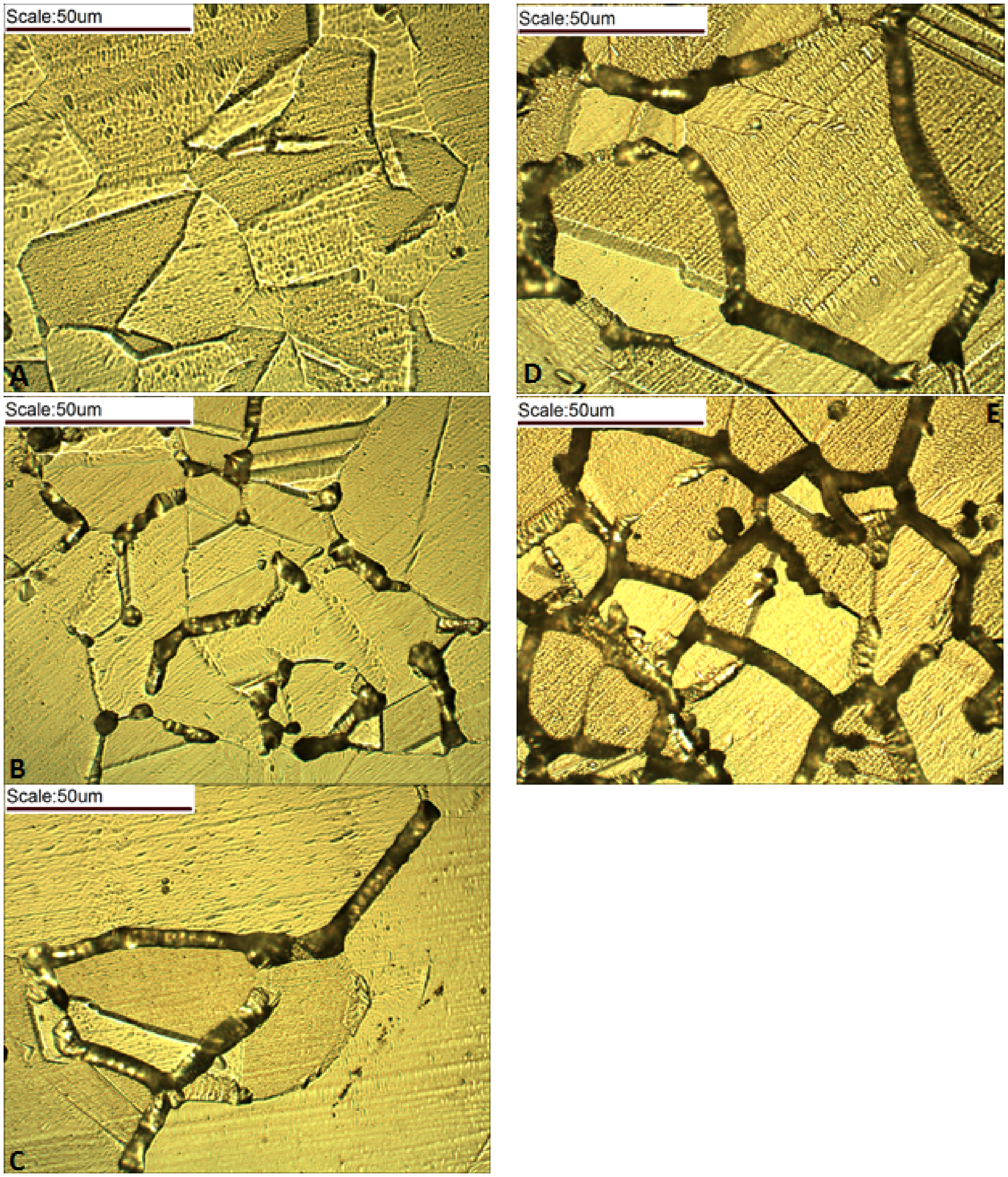

Figure 39: Microscopy for annealed SS304 samples at 0 minutes(A), 150 minutes (B), 180 minutes (C), 240 minutes (D) and 360 minutes (E)

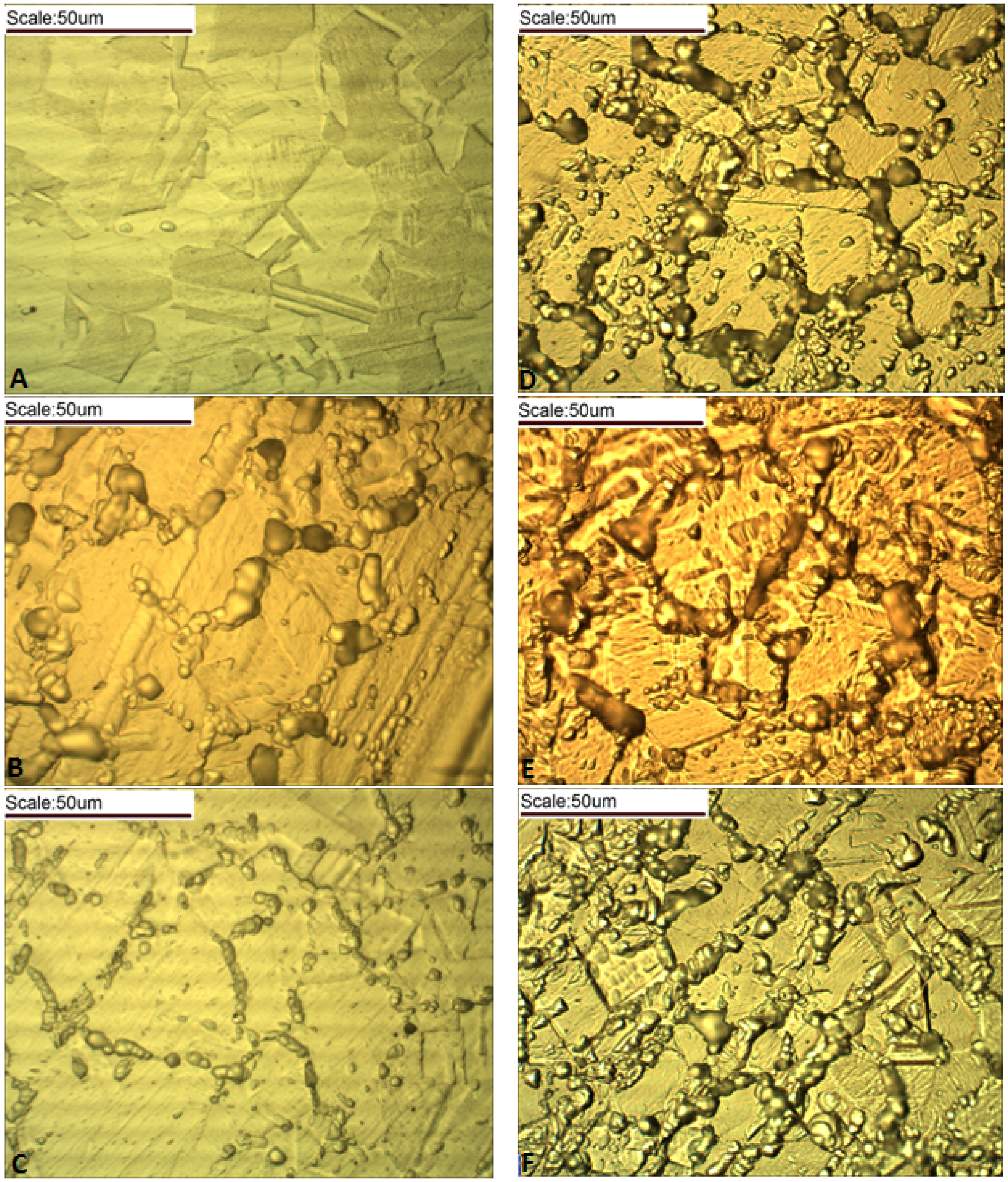

Figure 40: Microscopy for as-recieved SS304L samples at 0 minutes(A), 900 minutes (B), 1200 minutes (C), 1500 minutes (D), 2220 minutes (E) and 2520 minutes (F)

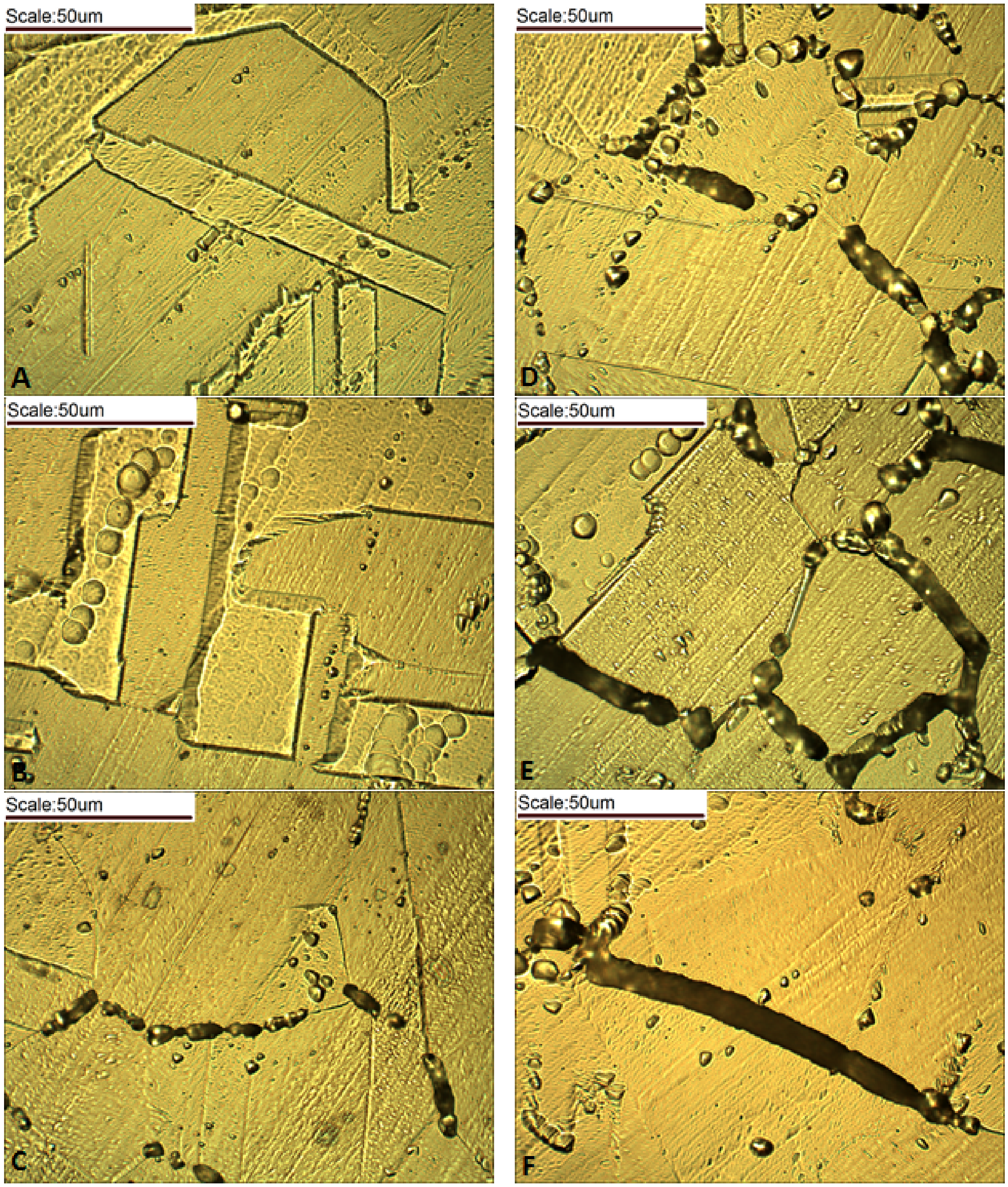

Figure 41: Microscopy for annealed SS304L samples at 0 minutes(A), 180 minutes (B), 480 minutes (C), 780 minutes (D), 1440 minutes (E) and 1800 minutes (F)

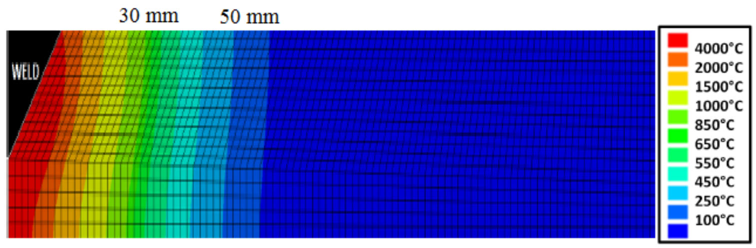

Figure 42: Heat-transfer FE-model

7.2 Results for Welded Specimen

7.2.1 Basics of the Welding Process

Lakocy [15] evaluated the thermal effect of welding to the material next to the weld axis with a finite element model. Figure 42 illustrates the maximum temperatures for different locations at a stainless steel plate. This figure shows the maximum temperature close to the weld axis of 4000 °C and a temperature 50 mm from the weld axis of 250 °C.

Many researchers investigated the effects of welding on the material properties. Ashby et al. [3] have examined the phase change in the heat affected zone. Figure 43 illustrates the different phase changes dependent on the temperature induced by welding. Close to the weld axis are a melt and a γ-phase. With decreasing temperature the melt-phase disappears and with a decrease of the temperature below 700 °C a α-phase gets induced.

Figure 44 shows the hoop and axial stresses over distance from the weld axis [16]. The peak value of the hoop stress is at the weld axis and decreases afterwards. At about 25 mm from the weld axis it starts increasing and reaches a steady state phase at 80 mm from the weld axis. The axial stress increases to its peak value at about 50 mm and decreases afterwards.

Different grain sizes effect the sensitization process as stated in section 2.2. Suarez et al. have shown that the grain size decreases from about 130 μm to 15 μm between 1.5 mm to 6 mm from the weld axis [27]. Furthermore, Schmidt et al. [26] have

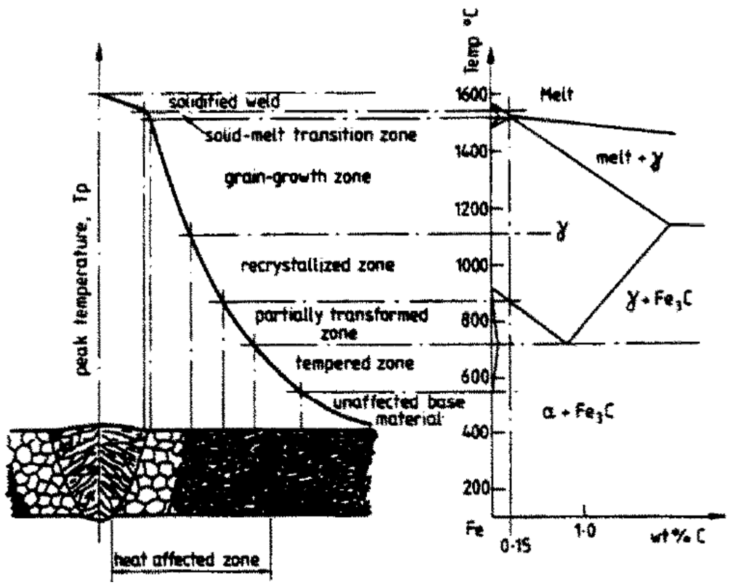

Figure 43: Phase changes occuring in the heat-affected zone of low carbon steel [3]

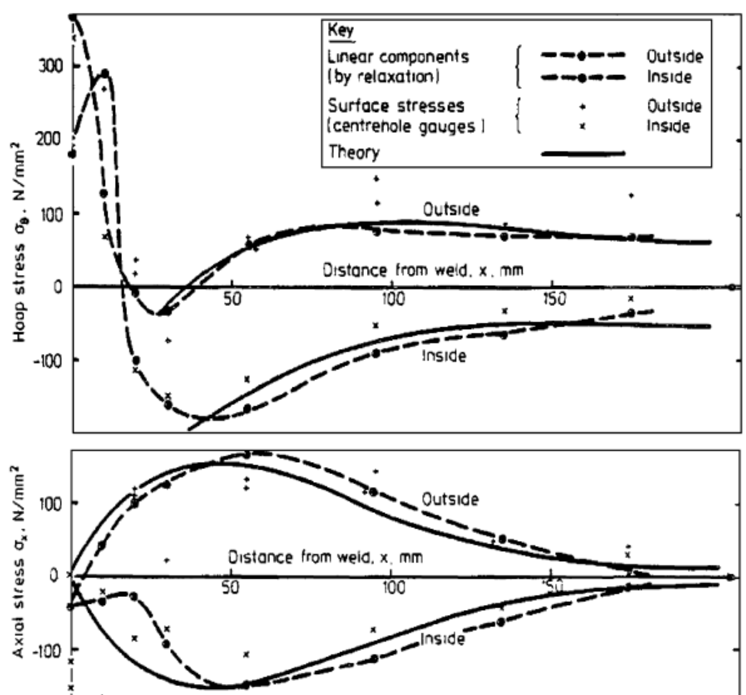

Figure 44: Hoop and residual stresses over distance from the weld axis [16]

mentioned that the material is over 550 °C within 0.3 cm from the weld joint for about 180 to 220 seconds. With a higher distance less than 30 seconds were spent at 550 °C. All these changes in the material properties, material composition and grain structure will effect the Rayleigh wave measurements. The following sections show the results for heat treated weld specimen. Heating times can be seen in table 5 .

7.2.2 Nonlinear Rayleigh Wave Measurement Results

Figure 45 illustrates the measured nonlinearity parameter β' over the distance from the weld axis for the as-recieved, 30 min heat treated and 210 minutes heat treated weld sample. It can be seen that the material nonlinearity increases with decreasing distance from the weld axis. All results are normalized to the result of the as-recieved 130 mm measurement. All three curves show the same trend at distances measured away from the weld axis. The β' curves follow a slow decrease at the beginning, a higher decrease in the middle and than a linear decrease at the end. The bigger error bars compared to the plate sample results are the result of a non-homogenous material. Therefore, we can see large variations between the different measurements. The averaged nonlinearity parameter β' of the 30 mm measurement is almost twice as large as the 110 mm β' for the as-recieved weld sample. The curve drops averagely by 30%. However, the drop does not occur evenly. The uneven drop might be caused by measurement uncertainties, or by microstructural changes occurring during the weld process as described in section 7.2 that influence the effect of the heat treatment as well. After the drop of the 30 minute heat treated weld sample, the curve for the 210 minutes heat treated weld sample rises between 10% and 30% compared to the 30 minutes heat treated weld sample. This is the same overall trend seen in the as-recieved plate samples as well. Figure 27 and figure 28 illustrate a drop and an increase of β' with longer heat treatment times. This observed behavior in β' is due to a combination of precipitates and other material effects.

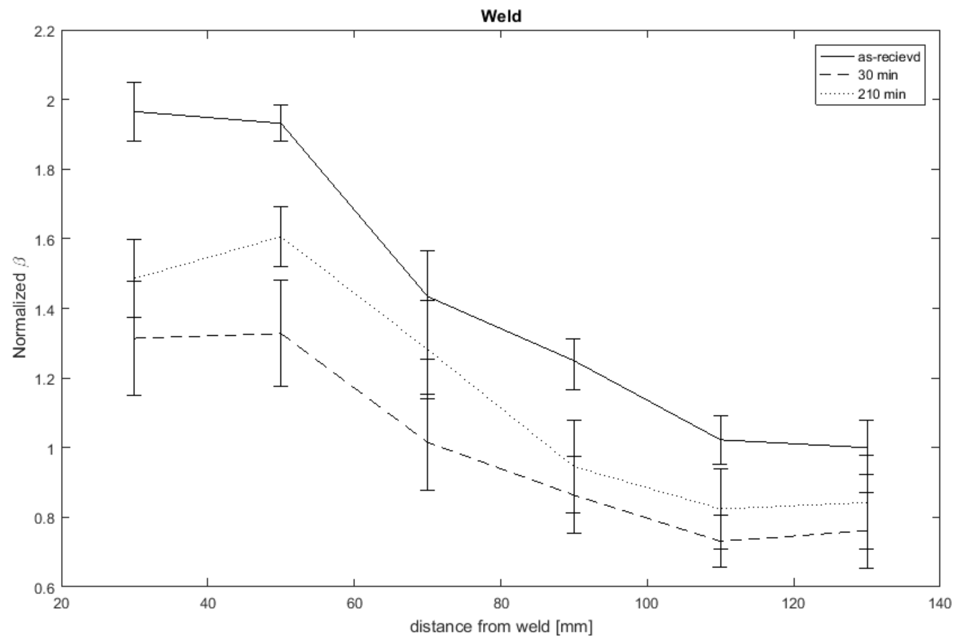

Figure 45: Normalized β' over distance from weld axis

7.2.3 EPR Results

Figure 46 shows the EPR results over the distance from the weld axis for the as-recieved, 30 minutes heat treated and 210 minutes heat treated weld sample. All results are normalized to the result of the as-recieved 130 mm. The current density stays the same over different distances from the weld for the as-recieved and the 30 minutes heat treated weld sample. However, the curve of the 30 minutes heat treated sample averagely increases by 230%. The variation between the different distances from the welding axis is either the result of the measurement uncertainty or different sizes of the chromium depleted zones. However, the overall variation is very small. The increase of the 210 minutes heat treated curve is between 440% and 490% compared to the as-recieved weld sample. Furthermore, this curve is almost linearly increasing with decreasing distance from the weld axis. This shows, that with decreasing distance to the weld axis the chromium depleted zones get bigger. This observed behavior leads to the assumption that the welding process either supports

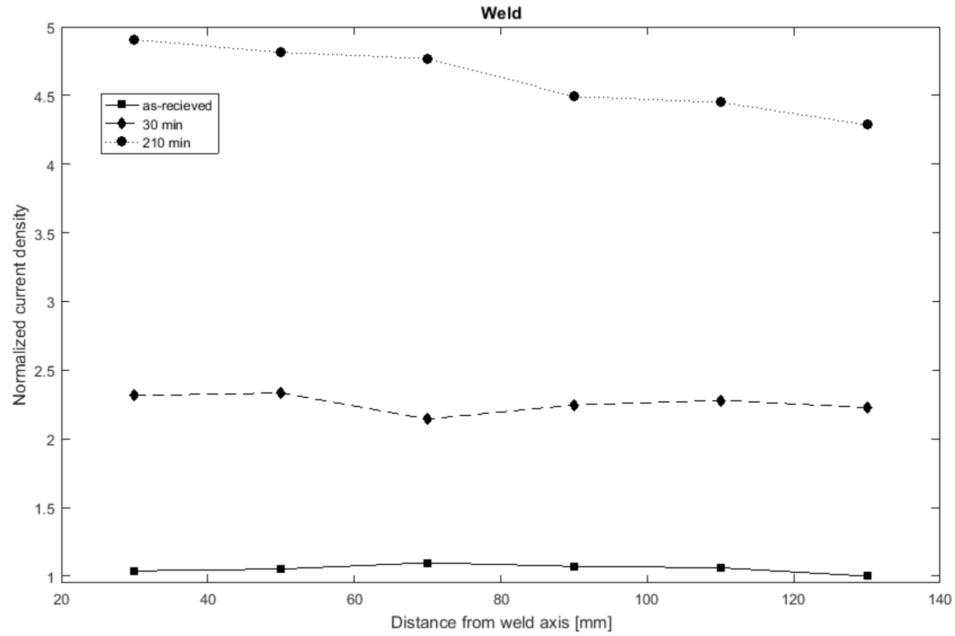

Figure 46: EPR results over distance from weld axis

the chromium carbide nucleation close to the weld axis or retard the nucleation with increasing distance to the weld axis.

7.2.4 Microscopy

Figure 47 presents the microscopy images for the different distances from the weld axis for the as-recieved weld specimen. It shows that there is no different between these pictures. Furthermore, there are no chromium carbide precipitates at the grain boundaries, which leads to the assumption that the increase of the nonlinearity parameter β' is only a result of a different dislocation density and microstructure caused by the welding process. Figure 48 illustrates the microscopy images over different distances from the weld axis for the 30 minutes heat treated weld specimen. These pictures don't show any chromium carbide precipitates and look the same for the different distances. Figure 49 shows the microscopy images over different distances from the weld axis for the 210 minutes heat treated weld specimen. It can be seen that the numbers and size of precipitates are smaller for increasing distance from the weld axis. 50 mm and 70 mm from the weld axis the size and number are the highest and 30 mm from the weld axis it decreases again. A new picture capturing software causes the different resolution and color of the figures 47 and 48 and figure 49.

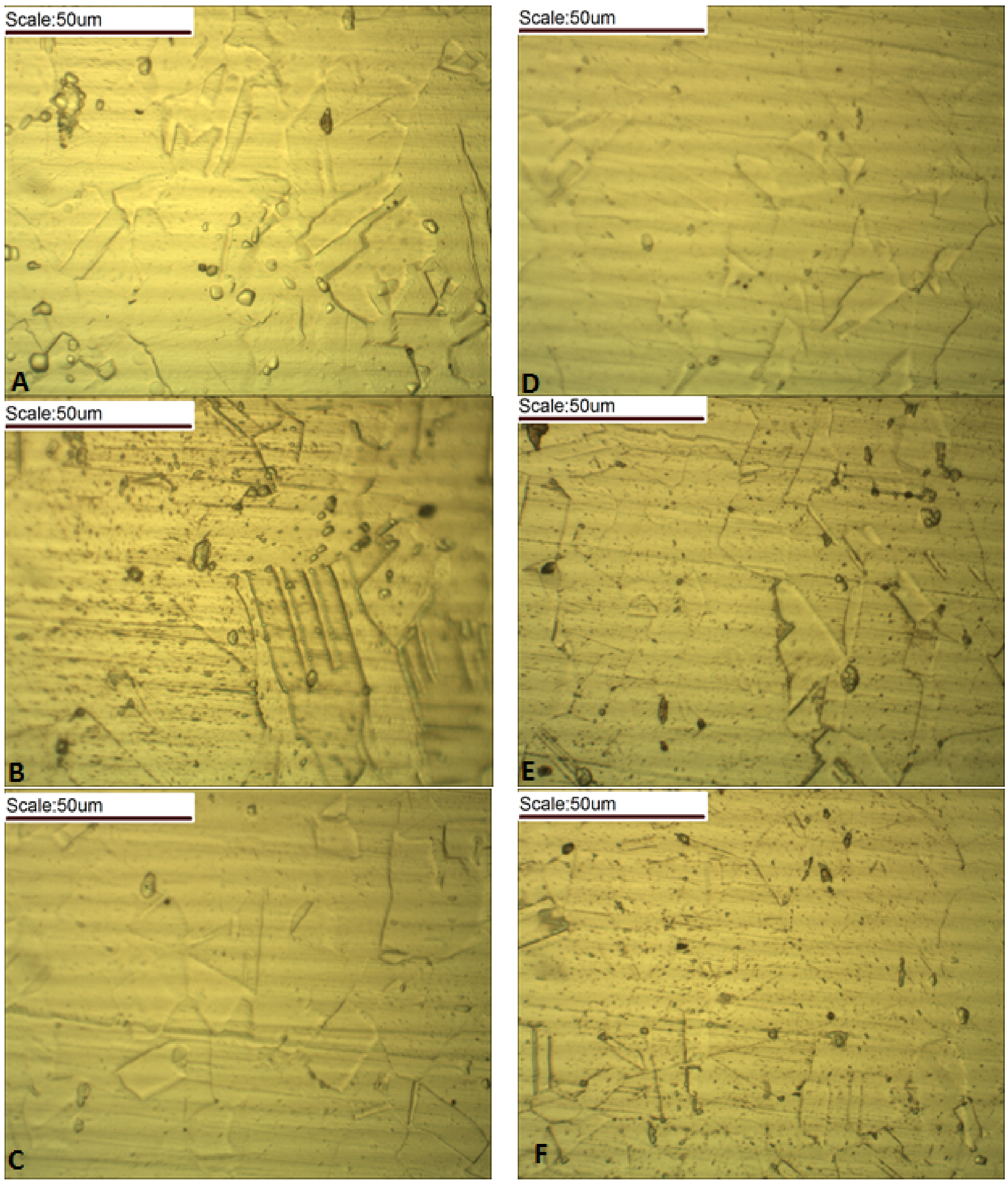

Figure 47: Microscopy for welded sample 130 mm (A), 110 mm (B), 90 mm (C), 70 mm(D), 50 mm (E) and 30 mm (F) from weld

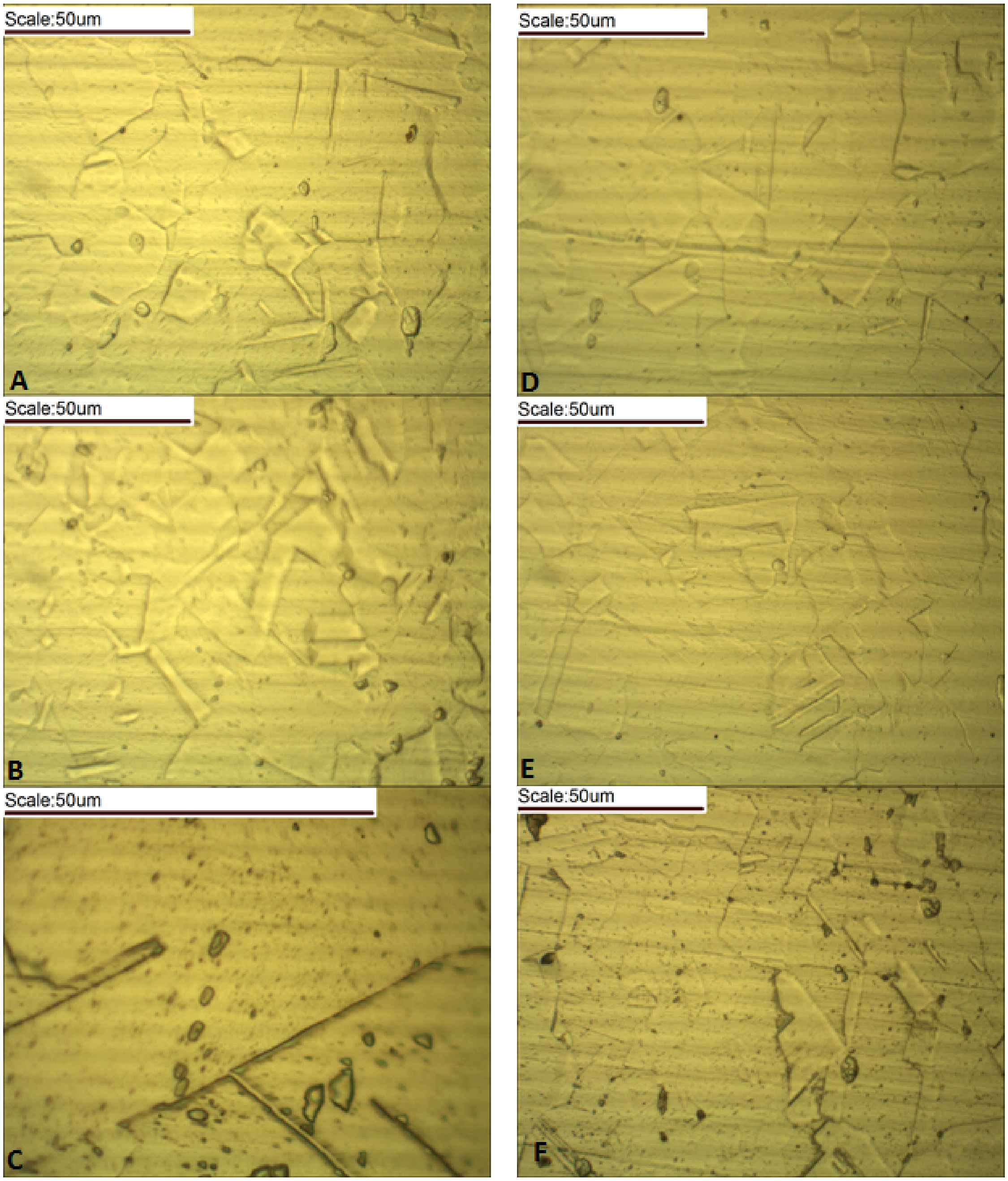

Figure 48: Microscopy for 30 minutes heat treated welded sample 130 mm (A), 110 mm (B), 90 mm (C), 70 mm(D), 50 mm (E) and 30 mm (F) from weld

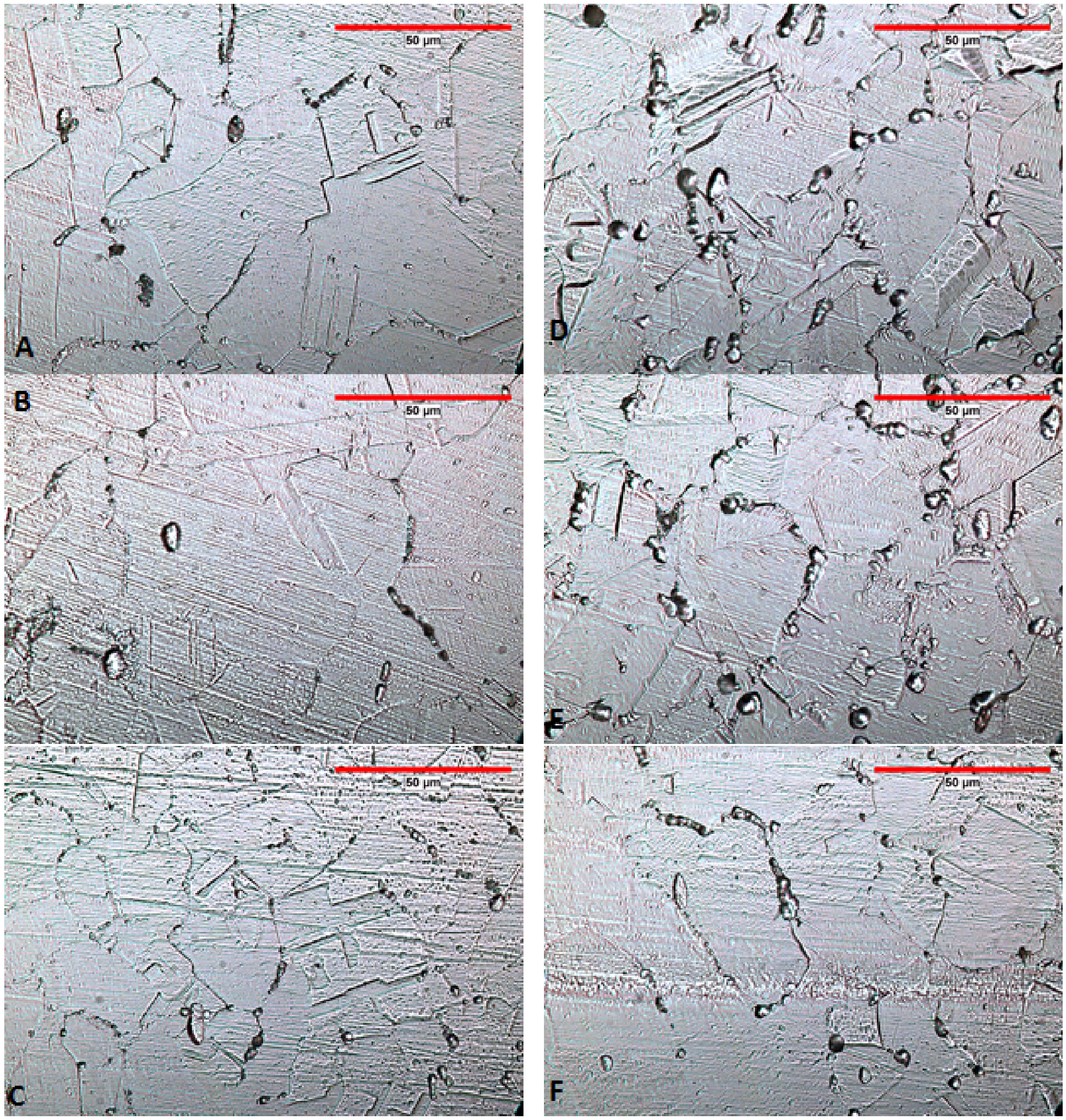

Figure 49: Microscopy for 210 minutes heat treated welded sample 130 mm (A), 110 mm (B), 90 mm (C), 70 mm(D), 50 mm (E) and 30 mm (F) from weld

7.3 Discussion

One of the main objectives of this research is to determine a relationship between the chromium carbide nucleation and the change of the nonlinearity parameter β'. Therefore, we have to correlate the nonlinearity parameter β' and the normalized current density with each other. Figure 50 illustrates the normalized β' values and

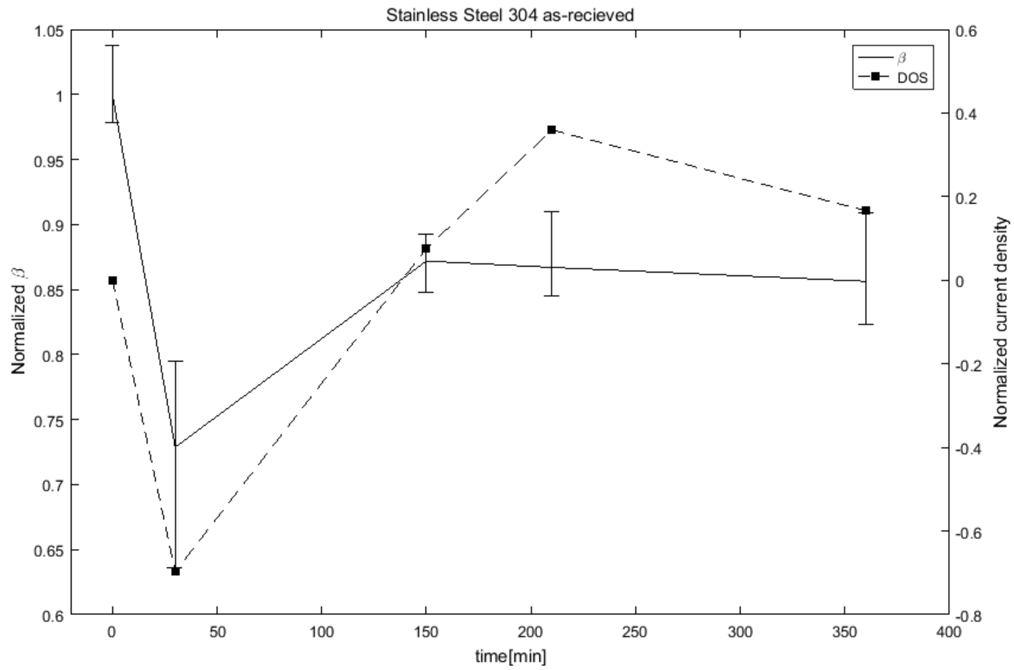

Figure 50: Normalized β' and normalized current density over heat treatment time for as-recieved SS304 samples

the normalized current density over different heat treatment times at 675 °C as-recieved SS304 samples. Between 30 minutes and 150 minutes β' increases by 14% and the current density increases by 73%. This leads to a 0.192% increase by β' per percentage increase of the current density.

Figure 51 represents the normalized β' values and the normalized current density over different heat treatment times at 675 °C for the as-recieved SS304L specimens. In this case, β' increases by 21% and the current density increases by 200% between 450 minutes and 1500 minutes. Therefore, this leads to a 0.105% increase by β' per percentage increase of the current density.

Figure 52 shows the normalized β' values and the normalized current density over different heat treatment times at 675 °C for the annealed SS304 samples. In this case, β' increases by 26% and the current density by 350%. Therefore, this leads to a 0.074% increase by β' per percentage increase of the current density.

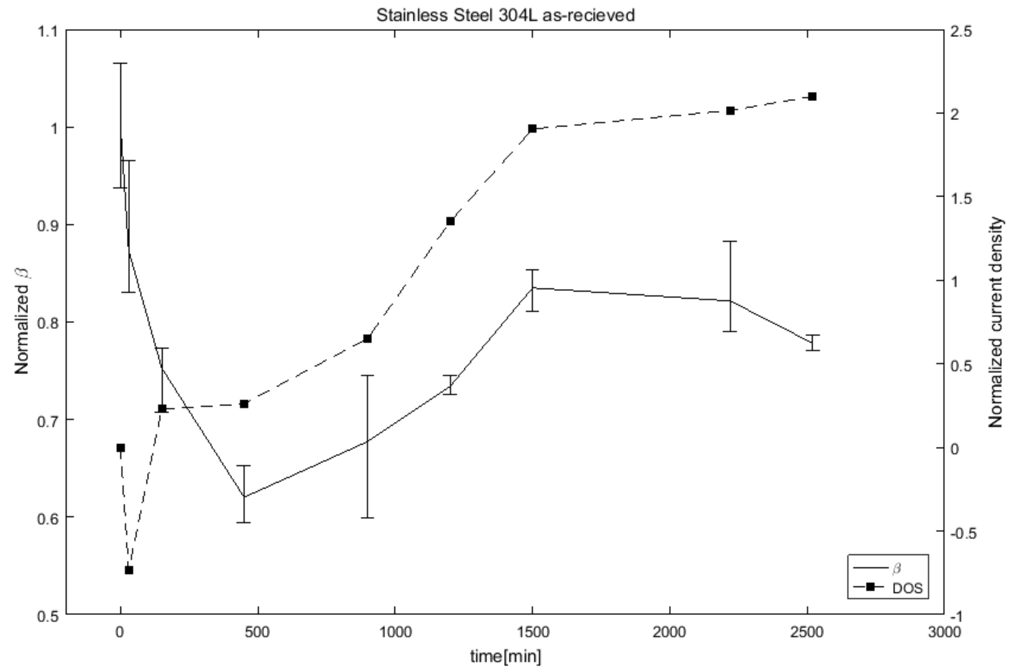

Figure 51: Normalized β' and normalized current density over heat treatment time for as-recieved SS304L samples

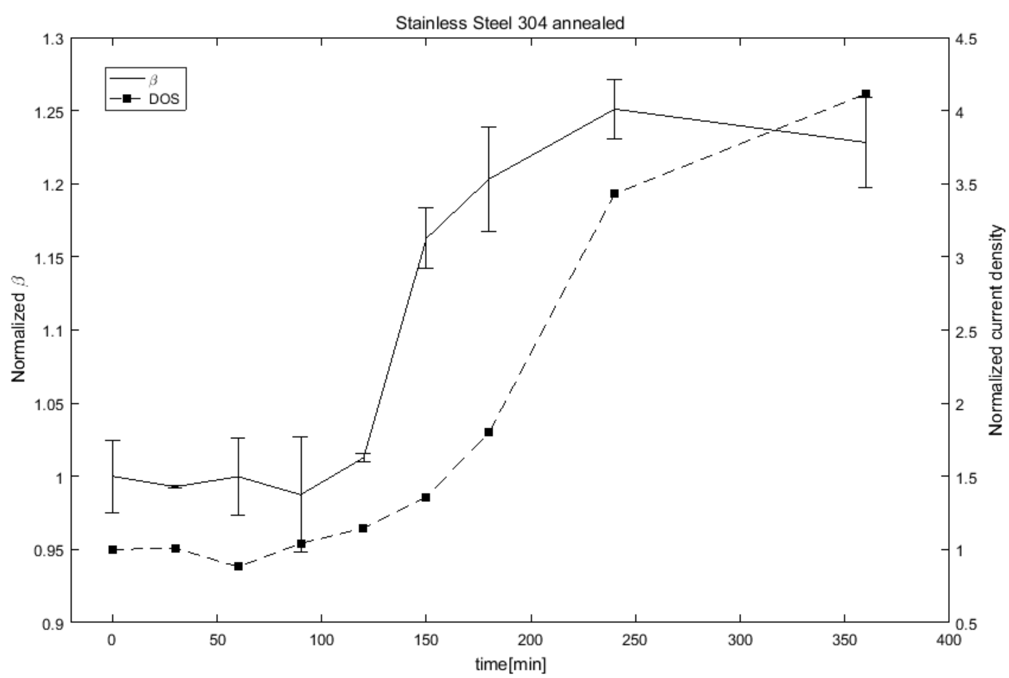

Figure 52: Normalized β' and normalized current density over heat treatment time for annealed SS304 samples

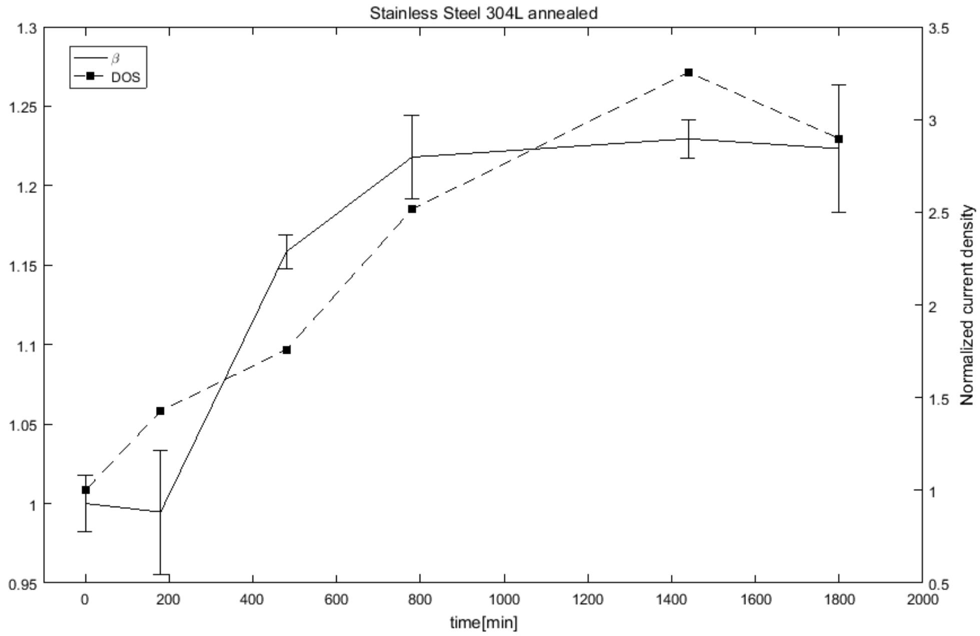

Figure 53: Normalized β' and normalized current density over heat treatment time for annealed SS304L samples

Figure 52 illustrates the normalized β' values and the normalized current density over different heat treatment times at 675 °C for the annealed SS304 samples. In this case, β' increases by 23 % and the current density increases by 320% between 180 and 1440 minutes. Therefore, this leads to a 0.071% increase by β' per percentage increase of the current density.

The range shows a variety from 0.071% to 0.192% increase in β' per percent increase in the current density. This range is too big to make a general assumption for every material. However, if we just look at the annealed samples the variety is just between 0.071 to 0.074. The annealed samples are less affected by prior cold work during the manufacturing process. This cold work affects the martensite phase formation, which contribute to the sensitization process. Therefore, the annealed samples represent sensitization results, that are not influenced by other effects such as dislocation reduction. Furthermore, the increase of both parameters is strongly dependent on the material and the current state of the samples as internal stresses

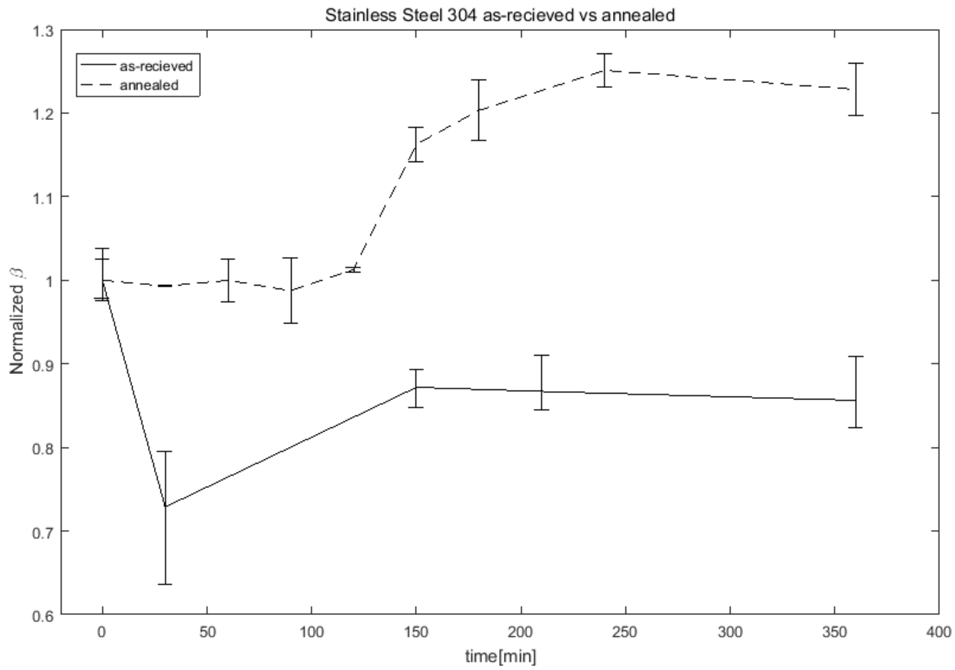

Figure 54: Normalized β' over heat treatment time for SS304L as-recieved and annealed samples

and number of dislocations influencing the Rayleigh wave measurements.

It is important to evaluate the difference between the as-recieved and the annealed samples, because pipeline parts or nuclear reactor parts are usually used as they get delivered from the manufacturing process to the facility. Figure 54 shows the normalized β' over different heat treatment times for the as-recieved and annealed samples of SS304. The main difference between the curves is the peak values of β'. For the annealed sample, the peak value is 11% higher than the as received material, which measures 25% higher. The reason for that could be the change in grain size for the annealed samples. A different number of dislocations and internal stresses could also be a reason for the different β' values. Furthermore, chromium carbide nucleation starts later for the annealed sample. This can be a grain size effect or a effect of prior cold work. This causes a longer travel time for the carbon to get to the grain boundaries and react with the chromium atoms.

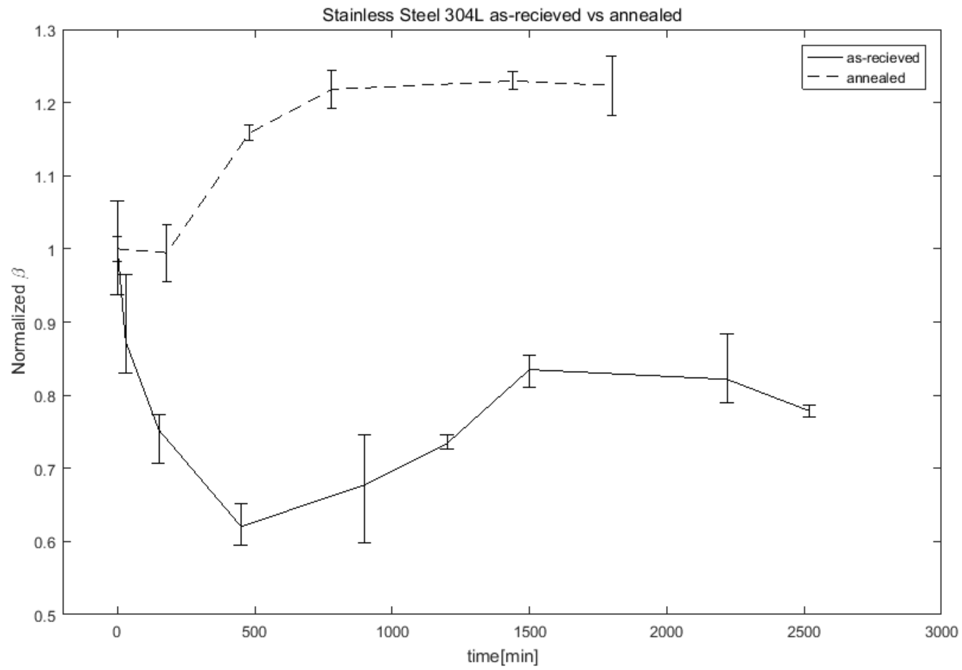

Figure 55: Normalized β' over heat treatment time for SS304L as-recieved and annealed samples

Figure (55) shows the normalized β' over different heat treatment times for the as-recieved and annealed samples of SS304L. There are also a differences between the peak values of β' for the as-recieved and annealed samples. The β' increase caused by precipitates is almost the same for both. Furthermore, chromium carbide nucleation starts earlier for the annealed sample. The high temperature during the annealing process accelerates the stress relieving process. Therefore, sensitization can start earlier.

Figure 45 illustrates the normalized nonlinearity parameter β' and figure 46 the normalized current density for the weld sample. The EPR results and the microscopy images of section 7.2.3 and 7.2.4 show that the increase in β' for the as-recieved and 30 minutes heat treated weld sample is not contributed by precipitates. Figure 47 and figure 48 don't show any precipitates. As already described in section 7.1.1, β' almost doubles its value for the as-recieved and the 30 minutes heat treated weld sample with decreasing distance from the weld axis. This increase is caused by dislocations, internal stresses and changes to γ and α phases and not necessarily the presence of precipitates. The increase of the current density for the 30 minutes heat treated weld sample compared to the as-recieved weld sample is caused by the start of the sensitization process. However, the chromium depleted zones are still to small to detect them with the nonlinear Rayleigh wave measurement setup or microscopy. Compared to the stainless steel plate specimens, the increase in β' for the weld sample is five times higher. Therefore, residual stresses, different material phases and dislocations affect the nonlinearity parameter β' more than chromium carbide precipitates. The nonlinearity parameter β' increases between 10 and 27% for the 210 minutes heat treated compared to the 30 minutes heat treated weld sample. However, the increase gets bigger for decreasing distance from the weld axis. Between 130 mm and 90 mm the increase is around 15%, about 25% for the 50 and 70 mm distance from the weld axis and drops again to 17% for the 30 mm measurement. This drop is either caused by measurement uncertainty or a decreasing number of precipitates. The EPR results show a linearly increase of the current density for decreasing distance from the weld axis for the 210 minutes heat treated weld specimen. However, figure 49 illustrates an increasing number and size of precipitates for decreasing distance from the weld axis. This shows that the welding process and all the microstructural changes in grain size, γ and α phases and internal stresses support the chromium carbide nucleation during the sensitization process. Compared to SS304 plate results, the weld specimen shows less precipitates for the distance between 90 mm and 130 mm. Here, the welding process retards the chromium carbide nucleation.

par In conclusion, the sensitization process is almost the same for the weld specimen compared to the plate specimen. The main difference is that the sensitization process is not the same over different distances from the weld axis. Therefore, the different temperature impacts during the welding process affect the sensitization process at 675 °C. Furthermore, the results show that there are no precipitates former the welding process, because the time where the material is at the right temperature for sensitization is to short as the results of the plate samples have shown.

CHAPTER VIII

CONCLUSION AND OUTLOOK

This chapter summarizes the results and gives a brief conclusion of this research work. Furthermore, possible future work in this research area is described.

8.1 Conclusion

This thesis describes the fundamentals of wave propagation in solids, including the nonlinear wave propagation of Rayleigh surface waves. Furthermore, it discusses stress corrosion cracking and sensitization, which is influenced by many different factors. The thesis outlines the test setups and test procedure for the nonlinear ultrasonic Rayleigh wave measurements and the EPR measurements. This research shows, that nonlinear ultrasound Rayleigh wave measurements are sensitive to the presence of chromium carbide precipitates in austenitic stainless steels. The results show that β' increases with an increasing sensitization time for the samples of the SS304 and SS304L. Since the SS304L consists of less carbon compared to SS304, the sensitization process takes about 5 times longer for the SS304L material. This behavior is seen by the longer time period it takes for β' to increase in the SS304L specimen. The research also considers the difference between annealed and not-annealed samples. Both samples show the same trend, where β' increases by chromium carbide nucleation. However, there is a decrease in β' at the beginning of the sensitization heat treatment for the as-recieved samples. This decrease in β' occurs because of a decrease of the number of dislocations and a reduction of internal stresses.

Both EPR results and microscopy support the described Rayleigh wave results for the annealed and as-recieved samples. The EPR results show an increase for the normalized current density with increasing heat treatment time. This increase is based on an increase of the chromium depleted zones around the grain boundaries. Chromium reacts with the carbon at the grain boundary and leaves chromium depleted zones behind which can be measured by the EPR test. Therefore, the EPR test activates the chromium depleted zones and measures the current density.

The weld sample shows an increase of β' of about 100% with decreasing distance away from the weld axis for the as-recieved and 30 minutes heat treated weld sample. However, the EPR results do not show any increase of the chromium depleted zones around the grain boundaries for the as-recieved and 30 minutes heat treated weld sample. Furthermore, the microscopy images do not show any chromium carbide precipitates. Therefore, the increase in β' occurs mainly because of residual stresses, different α and γ-phases, different grain sizes and dislocations and not from chromium carbide nucleation. Compared to the SS304 plate samples the increase in β' for the welded sample is five times higher. This leads to the conclusion that residual stresses, different material phases and dislocations affect the nonlinearity parameter β' more than chromium carbide precipitates. With increasing heat treatment time chromium carbide precipitates affect the Rayleigh wave and EPR measurements. It can be seen that the precipitate growth gets retarded with increasing distance from the weld axis. Therefore, the welding process affects the sensitization process during the heat treatment.

8.2 Outlook

This research shows the feasibility of nonlinear ultrasonic Rayleigh wave measurements to detect chromium carbide precipitates and other micro-structural changes. However, the measurement uncertainty of the used measurement setup can be improved. The influence of uncertainties like clamp forces or the amount of oil used for each measurement should be decreased. Therefore, pressure sensors could be used to evaluate the clamp forces in future research works. This would make the measurements more reproducible. Furthermore, further development steps for the measurement setup have to be done to develop a measurement setup that can be used in the field.

It is necessary to extend our knowledge about sensitization in the HAZ of welded materials. The results for weld-sensitization in this research provides a trend of chromium carbide nucleation in the HAZ of the weld. However, it is necessary to evaluate it as carefully as we investigated the sensitization process for the stainless steel plate samples, because the shown results are affected by a lot of microstructural changes. Therefore, we have to look at annealed samples as well to reduce the effects of prior cold work from the manufacturing process. Looking at as-recieved samples gives us a good insight about the material behavior in the field. However, to understand the behavior of the materials based on sensitization it is necessary to put them on a common baseline by annealing.

REFERENCES

[1] Abraham, S. T., Albert, S., Das, C., Parvathavarthini, N., Venkatraman, B., Mini, R., and Balasubramaniam, K., "Assessment of sensitization in aisi 304 stainless steel by nonlinear ultrasonic method," *Acta Metallurgica Sinica (English Letters)*, vol. 26, no. 5, pp. 545–552, 2013.

[2] Aschenbach, J., *Wave propagation in elastic solidsAssessment of Stress Corrosion Cracking on Pipeline Steels Weldments Used in the Petroleum Industry by Slow Strain Rate Tests*. North-Holland, 1999.

[3] Ashby, M. and Easterling, K. E., "A first report on diagrams for grain growth in welds," *Acta metallurgica*, vol. 30, no. 11, pp. 1969–1978, 1982.

[4] ASTM, "G108-94 standard test method for electrochemical reactivation (epr) for detecting sensitization of aisi type 304 and 304l stainless steels," 1994.

[5] ASTM, "E407-07 standard practice for microetching metals and alloys," 2015.

[6] Beltran, R., Maldonado, J., Murr, L., and Fisher, W., "Effects of strain and grain size on carbide precipitation and corrosion sensitization behavior in 304 stainless steel," *Acta materialia*, vol. 45, no. 10, pp. 4351–4360, 1997.

[7] Chung, P. and Szklarska-Smialowska, S., "The effect of heat treatment on the degree of sensitization of type 304 stainless steel," *Corrosion*, vol. 37, no. 1, pp. 39–50, 1981.

[8] Contreras, A., Albiter, A., Salazar, M., Vega, O., and Galván, R., *Assessment of Stress Corrosion Cracking on Pipeline Steels Weldments Used in the Petroleum Industry by Slow Strain Rate Tests*. INTECH Open Access Publisher, 2011.

[9] Garcia, C., Martin, F., De Tiedra, P., Heredero, J., and Aparicio, M., "Effect of prior cold work on intergranular and transgranular corrosion in type 304 stainless steels: quantitative discrimination by image analysis," *Corrosion*, vol. 56, no. 3, pp. 243–255, 2000.

[10] Hamilton, M. and Blackstock, D., *Nonlinear Acoustics*. Academic Press, 1998.

[11] Herrmann, J., Kim, J.-Y., Jacobs, L. J., Qu, J., Littles, J. W., and Savage, M. F., "Assessment of material damage in a nickel-base superalloy using nonlinear rayleigh surface waves," *Journal of Applied Physics*, vol. 99, no. 12, p. 124913, 2006.

[12] Kim, J.-Y., Jacobs, L. J., Qu, J., and Littles, J. W., "Experimental characterization of fatigue damage in a nickel-base superalloy using nonlinear ultrasonic waves," *The Journal of the Acoustical Society of America*, vol. 120, no. 3, pp. 1266–1273, 2006.

[13] Kina, A. Y., Souza, V., Tavares, S., Pardal, J., and Souza, J., "Microstructure and intergranular corrosion resistance evaluation of aisi 304 steel for high temperature service," *Materials characterization*, vol. 59, no. 5, pp. 651–655, 2008.

[14] Kokawa, H., Shimada, M., and Sato, Y. S., "Grain-boundary structure and precipitation in sensitized austenitic stainless steel," *JOM*, vol. 52, no. 7, pp. 34–37, 2000.

[15] Lakocy, A. J., "Experimental characterization of stress corrosion cracking sensitization in austenitic stainless steel using nonlinear ultrasonic rayleigh waves," Master's thesis, Georgia Institute of Technology, 2015.

[16] Leggatt, R., "Residual stresses in welded structures," *International Journal of Pressure Vessels and Piping*, vol. 85, no. 3, pp. 144–151, 2008.

[17] Marino, D., Kim, J.-Y., Ruiz, A., Joo, Y.-S., Qu, J., and Jacobs, L. J., "Using nonlinear ultrasound to track microstructural changes due to thermal aging in modified 9% cr ferritic martensitic steel," *NDT & E International*, vol. 79, pp. 46–52, 2016.

[18] Matlack, K., Kim, J.-Y., Jacobs, L., and Qu, J., "Review of second harmonic generation measurement techniques for material state determination in metals," *Journal of Nondestructive Evaluation*, vol. 34, no. 1, pp. 1–23, 2015.

[19] Morlock, F., "Evaluation of stress corrosion cracking in sensitized 304 stainless steel using nonlinear rayleigh waves," Master's thesis, Georgia Institute of Technology, 2014.

[20] Norris, A., "Symmetry conditions for third order elastic moduli and implications in nonlinear wave theory," *Journal of elasticity*, vol. 25, no. 3, pp. 247–257, 1991.

[21] Parvathavarthini, N. and Dayal, R., "Time–temperature-sensitization diagrams and critical cooling rates of different nitrogen containing austenitic stainless steels," *Journal of Nuclear Materials*, vol. 399, no. 1, pp. 62–67, 2010.

[22] Parvathavarthini, N., Mulki, S., Dayal, R., Samajdar, I., Mani, K., and Raj, B., "Sensitization control in aisi 316l (n) austenitic stainless steel: defining the role of the nature of grain boundary," *Corrosion Science*, vol. 51, no. 9, pp. 2144–2150, 2009.

[23] Parvathavarthini, N. and Mudali, U. K., "Electrochemical techniques for estimating the degree of sensitization in austenitic stainless steels," *Corrosion Reviews*, vol. 32, no. 5-6, pp. 183–225, 2014.

[24] Pascali, R., Benvenuti, A., and Wenger, D., "Carbon content and grain size effects on the sensitization of aisi type 304 stainless steels," *Corrosion*, vol. 40, no. 1, pp. 21–32, 1984.

[25] Pruell, C., Kim, J.-Y., Qu, J., and Jacobs, L., "A nonlinear-guided wave technique for evaluating plasticity-driven material damage in a metal plate," *Ndt & E International*, vol. 42, no. 3, pp. 199–203, 2009.

[26] Schmidt, C. G., Caligiuri, R. D., Eiselstein, L. E., Wing, S. S., and Cubicciotti, D., "Low temperature sensitization of type 304 stainless steel pipe weld heat affected zone," *Metallurgical Transactions A*, vol. 18, no. 8, pp. 1483–1493, 1987.

[27] Suárez, J., Molleda, F., and de Salazar, J. G., "Modeling of grain growth during arc welding of high strength low alloy steels," *Materials characterization*, vol. 28, no. 1, pp. 3–13, 1992.

[28] Thiele, S., "Air-coupled detection of rayleigh surface waves to assess material nonlinearity due to precipitation in alloy steel," Master's thesis, Georgia Institute of Technology, 2013.

[29] Thiele, S., Torello, D., Matlack, K. H., Kim, J.-Y., Qu, J., and Jacobs, L. J., "Diffraction, attenuation, and source corrections for nonlinear rayleigh wave ultrasonic measurements," *Ultrasonics*, vol. 56, pp. 417–426, 2015.

[30] Torello, D. E., Kim, J.-Y., Qu, J., and Jacobs, L. J., "Characterization of air-coupled ultrasonic receivers for nonlinear rayleigh wave nondestructive evaluation," *The Journal of the Acoustical Society of America*, vol. 138, no. 3, pp. 1837–1837, 2015.

[31] Trillo, E., Beltran, R., Maldonado, J., Romero, R., Murr, L., Fisher, W., and Advani, A., "Combined effects of deformation (strain and strain state), grain size, and carbon content on carbide precipitation and corrosion sensitization in 304 stainless steel," *Materials Characterization*, vol. 35, no. 2, pp. 99–112, 1995.

[32] Trillo, E. and Murr, L., "Effects of carbon content, deformation, and interfacial energetics on carbide precipitation and corrosion sensitization in 304 stainless steel," *Acta Materialia*, vol. 47, no. 1, pp. 235–245, 1998.

[33] Viktorov, I., *Rayleigh and Lamb waves:physical theory and applications*. New York: Plenum Press, 1967.

[34] Viswanath, A., Rao, B., Mahadevan, S., Jayakumar, T., and Raj, B., "Microstructural characterization of m250 grade maraging steel using nonlinear ultrasonic technique," *Journal of materials science*, vol. 45, no. 24, pp. 6719–6726, 2010.

[35] Walker, S. V., Kim, J.-Y., Qu, J., and Jacobs, L. J., "Fatigue damage evaluation in a36 steel using nonlinear rayleigh surface waves," *NDT & E International*, vol. 48, pp. 10–15, 2012.

[36] Zeitvogel, D. T., Matlack, K. H., Kim, J.-Y., Jacobs, L. J., Singh, P. M., and Qu, J., "Characterization of stress corrosion cracking in carbon steel using nonlinear rayleigh surface waves," *Ndt & E International*, vol. 62, pp. 144–152, 2014.